

WASHINGTON UNIVERSITY IN ST. LOUIS

Division of Biology and Biomedical Sciences
Immunology

Dissertation Examination Committee:

Marco Colonna, Chair

John Cirrito

Brian Edelson

Gwendalyn Randolph

Gregory Wu

Regulation and Function of TREM2-dependent Pathways in Neurodegeneration

by

Wilbur Madison Song

A dissertation presented to
The Graduate School
of Washington University in
partial fulfillment of the
requirements for the degree
of Doctor of Philosophy

May 2020
St. Louis, Missouri

Table of Contents

List of Figures	iii
List of Tables	iv
Acknowledgments.....	v
Abstract	vi
Chapter 1: Introduction	1
1.1 Microglia at rest	1
1.2 A common microglial response to neuropathology	3
1.3 Functions of DAM during neurodegenerative disease	7
1.4 Genetic implication of microglia in neurodegeneration	13
1.5 Rationale for TREM2 study	19
Chapter 2: Impact of TREM2 variants on TREM2 function <i>in vitro</i> and <i>in vivo</i>	21
2.1 <i>In vitro</i> characterization of TREM2 variants	22
2.2 <i>In vivo</i> characterization of R47H variant	24
Chapter 3: TREM2-dependent pathways in activated microglia	40
3.1 The role of TREM2 in microglia energy metabolism	41
3.2 Role of Bhlhe40 upregulation in microglial activation	44
Chapter 4: Unbiased screen for TREM2 expression-modifying genes	55
4.1 Design and execution of CRISPR-Cas9 knockout screen	55
4.2 <i>In vitro</i> characterization of TMEM131 effect on TREM2	58
Chapter 5: Materials and methods	65
5.1 Methods for Chapter 2	65
5.2 Methods for Chapter 3	74
5.3 Methods for Chapter 4	79
References	82

List of Figures

Figure 1. TREM2 variants affect ligand binding in a reporter cell assay.	31
Figure 2. CV and R47H transgenes are specifically expressed in myeloid cell populations at comparable levels.	33
Figure 3. R47H exhibits reduced microglia numbers relative to CV.	34
Figure 4. CV and R47H transgenes do not affect A β accumulation in the cortex or hippocampus.	35
Figure 5. CV-KO-5XFAD mice have increased microglia activation compared to R47H-KO-5XFAD and KO-5XFAD mice.	36
Figure 6. CV-KO-5XFAD shows unique localization of soluble hTREM2 to neurons, plaques, and other non-microglial spaces.	38
Figure 7. Various immunostimulatory signals induce similar CV and R47H hTREM2 cleavage from the cell surface.	39
Figure 8. TREM2-deficient BMDMs show increased sensitivity of mTOR-dependent cell functions to growth factor deprivation.	47
Figure 9. TREM2-deficient microglia exhibit suppressed mTOR activity and increased autophagy in vivo in the 5xFAD model.	48
Figure 10. Alternative pathways can compensate for sensitivity to CSF-1 deprivation associated with TREM2 deficiency.	49
Figure 11. Cyclocreatine treatment partially restores microglia function in TREM2-deficient 5XFAD mice.	50
Figure 12. Bhlhe40-EGFP reporter mice have little Bhlhe40 expression in microglia.	52
Figure 13. Bhlhe40 deficiency does not affect activation state of sorted microglia on the transcriptional level.	53
Figure 14. Microglia and astrocyte clustering around plaques is altered by Bhlhe40 deficiency.	54
Figure 15. Statistically significant genes were validated by generating sgRNA knockouts using the top-ranking sgRNA from the screen.	62
Figure 16. TMEM131 suppresses surface levels of TREM2 through a metalloproteinase-independent mechanism.	63
Figure 17. TMEM131 suppression of TREM2 does not involve faster degradation rate or require the intramembranous charge interactions of TREM2 and DAP12.	64

List of Tables

Table 1. TREM2 gene variants found in the NIMH family-based WGS data and tested for replication in the ADSP case-control samples.....	32
Table 2. Genes upregulated in 8 month 5xFAD microglia compared to controls.	51
Table 3. List of genes and modified rank mean for statistically significant genes enriched in TREM2-low or TREM2-high fractions.	61

Acknowledgments

This work was supported by grants to Marco Colonna from the National Institutes on Aging (RF1 AG05148501) and the Cure Alzheimer's Fund. Microarray analysis was performed through the Genome Technology Access Center in the Department of Genetics at Washington University School of Medicine. Confocal microscopy was performed through the use of the Washington University Center for Cellular Imaging. Generation of transgenic mice was performed with the help of the Mouse Genetics Core at Washington University School of Medicine with partial support from NIH grants P30DK052574 and P30DK020579. We would like to thank Drs. Jason Ulrich, David Holtzman, and Maxim Artyomov for insightful discussions. We would also like to thank all members of the Colonna lab for offering invaluable support and guidance. We offer special thanks to the Washington University School of Engineering for allowing us to use their dissertation and thesis template as a starting point for the development of this document.

Wilbur M. Song

Washington University in St. Louis

May 2020

ABSTRACT OF THE DISSERTATION

Regulation and Function of TREM2-dependent Pathways in Neurodegeneration

by

Wilbur M. Song

Doctor of Philosophy in Biology and Biomedical Sciences

Immunology

Washington University in St. Louis, 2020

Professor Marco Colonna, Advisor

Carriers of the R47H allele of the microglia-specific lipid receptor TREM2 have a greatly increased risk of developing Alzheimer's disease. The objective of this dissertation is to develop further mechanistic knowledge about how TREM2 is regulated and how TREM2 mutations affect microglia and neurodegeneration. Using an *in vitro* reporter assay, we find that several AD risk-associated TREM2 mutations decrease ligand-dependent activation. Using humanized TREM2 mice, we find that *in vivo*, the R47H mutation leads to reduced microglia activation and response to A β , as well as decreased shedding of soluble TREM2. These results suggest that TREM2 is protective during disease. We find that TREM2-deficient macrophages *in vitro* are more susceptible to stress-induced loss of mTOR signaling, increased autophagy, and low-energy status. *In vivo*, microglia similarly fail to maintain mTOR signaling and increase autophagy in an A β mouse model, which could be rescued by enhancing energy utilization with long-term cyclocreatine supplementation. These results suggest that TREM2 is playing a fundamental role in maintaining microglia health and survival rather than triggering a specific activation signature. Finally, we perform an unbiased CRISPR-Cas9 knockout screen to identify and characterize

pathways that regulate TREM2 surface expression, identifying TMEM131 as a suppressor of TREM2 surface expression. We further demonstrate that TMEM131 regulation of TREM2 does not involve cleavage or degradation of TREM2 from the cell surface or require the unique intramembranous charge of TREM2. These results provide a stepping stone for identifying novel therapeutic targets related to TREM2.

Chapter 1: Introduction

1.1 Microglia at rest

Studies of the role of the immune system in neurological diseases have long been confined to grossly neuroinflammatory conditions such as infection, stroke, and certain autoimmune diseases. However, emerging evidence implicates immune function in a variety of chronic neurodegenerative diseases¹⁻⁵. In these cases, immune responses do not feature profuse inflammatory infiltrates but rather local responses by resident cells. While neurons and astrocytes do respond to various cytokines, the primary dedicated immune cell and most likely coordinator of immune responses in the central nervous system (CNS) is the microglia, an embryonically derived⁶, self-renewing⁷⁻⁹ tissue macrophage. In addition to other common myeloid lineage factors such as PU.1¹⁰, microglia maturation requires the lineage-specific transcription factors Irf8¹¹ and Sall1¹² and input from the gut microbiota^{13,14} and CNS microenvironment. The confluence of these factors generates a unique transcriptional signature, including surface receptors such as P2ry12, Fcrls, Siglec H, Tmem119, and Trem2; and transcription factors such as Sall1, Sall3, Zfp691, and Smad7. As with other tissue macrophages, microglia also express CX3CR1, Mer, and Fcgr1¹⁵. Recent studies examining isolated live human microglia for the first time revealed overall similarity between mouse and human microglia, with higher expression of some immune activation-associated genes such as MHCII, which may reflect genetically encoded or experiential differences^{16,17}.

To maintain their unique transcriptional identity, microglia require continuous signals from the microenvironment, as evidenced by the observation that culturing primary adult

microglia rapidly downregulates key microglia genes on the transcriptional and protein level¹⁷⁻¹⁹. One of the brain-derived signals required for the microglia signature is TGF β , as demonstrated by genetic TGF β deficiency studies, and supplementing cultured microglia with TGF β can partially restore microglia-specific gene expression^{12,18}. Recent attempts to differentiate microglia from pluripotent stem cells found that coculturing stem cell-derived microglia with neurons and astrocytes could achieve greater similarity to microglia *in situ*²⁰⁻²², suggesting that a complex mixture of cell-cell interactions and paracrine signaling shapes the microglia identity. Notably, the brain microenvironment is also not sufficient to fully recapitulate microglia gene expression, as peripherally monocytes forced to enter the brain do not fully adopt the homeostatic microglia signature^{23,24}. During homeostatic conditions, the tight dependence on microenvironment leads to subtle differences between microglia in different brain regions²⁵. However, in settings of neuropathology, the brain microenvironment becomes highly perturbed locally, and this could lead both to positive and negative signals that activate microglia. TGF β is classically thought of as an anti-inflammatory cytokine, and loss of TGF β signaling would be expected not only to disrupt the resting microglia signature but also to promote inflammatory responses by microglia. The enhanced understanding of fundamental microglia biology during development and homeostasis over the past few years has helped to contextualize microglia responses to pathological insults. Thus, while “microgliosis” has long been noted as a component of neuropathology, more mechanistic models of microglia function during disease are only now being fleshed out.

1.2 A common microglial response to neuropathology

Microglia proliferate and change morphology in response to neurodegenerative disease, a process referred to as “microgliosis”. In post-mortem Alzheimer’s disease (AD) specimens, reactive microglia are found in abundance surrounding amyloid beta (A β) plaques²⁶, and recent -omics studies in human brain have revealed that microglial changes constitute the strongest transcriptional and epigenetic signal of AD and normal aging^{27–30}. Reactive microglia also increase in Parkinson’s disease³¹ (PD) and Huntington’s disease (HD) brains^{32,33}. Accordingly, animal models of both amyloid accumulation and tauopathy, the two pathological hallmarks of AD, feature similar changes in the microglia population^{34,35}, as do MPTP-induced parkinsonism³⁶ and amyotrophic lateral sclerosis (ALS)³⁷ models. For many years, these degeneration- or disease-associated microglia (DAM) were vaguely described as having less ramified, more amoeboid morphology and expressing general macrophage activation markers such as MHCII and CD11c. The development of techniques to isolate microglia and perform genome-wide transcriptomic analysis has allowed finer characterization of DAM³⁸. Remarkably, DAM have a conserved transcriptional signature across standard neurodegeneration mouse models including A β -driven APP-Swe/PS1dE9 and 5XFAD mice^{39–41}, the P301S model of tauopathy⁴², the SOD1^{G93A} model of ALS⁴³, and the CK-p25 AD model⁴⁴. This signature includes both classical M1 and M2 genes, as well as interferon response, stress response, lysosome, and lipid metabolism modules. Upregulated genes include *Axl*, *Clec7a*, *Cst7*, *Spp1*, *Gpnmb*, *Lgals3*, *Apoe*, and *Trem2*, among many others. Surface proteins such as CD11c, MHCII, CD44, CD14, CD86, CD39, CD90, and CD274 (PD-L1) are also upregulated in DAM and have been validated on the protein level by mass cytometry^{45,46}. Conversely, homeostatic microglia signature genes are downregulated.

Although shared between neurodegeneration models, the DAM signature is not simply a generalized response to any stimulus. Microglia populations during experimental autoimmune encephalitis, which involves profuse inflammatory infiltrates, have distinct surface marker, cytokine, and signaling profiles compared to neurodegeneration models^{45,46}; and systemic lipopolysaccharide (LPS) injection, which causes acute neuroinflammation, leads to an overall different signature⁴⁷. Several meta-analyses of microglia gene expression datasets have also pointed out distinctions between neuroinflammatory and neurodegenerative microglia responses^{42,47}.

One important question is whether the DAM compartment consists of a single cell state or of multiple distinct populations of M1, M2, and other subsets. Single-cell RNA-seq analysis of microglia in 5XFAD and CK-p25 mice showed that DAM coordinately acquire the entire DAM signature and form a heterogeneous but nonetheless singular population by unbiased clustering analysis^{44,48}. Subset analysis of DAM has also been informed by several large-scale mass cytometry studies. While these studies were powerful enough to distinguish meningeal macrophages, perivascular macrophages, and peripheral monocytes in addition to microglia, they also failed to identify multiple subsets of DAM^{45,46}. One study did distinguish relatively minor subsets of CD44⁺ and CXCR4⁺ DAMs by flow cytometry, arguing for segregation of at least some DAM modules⁴⁹. Moreover, in the CK-p25 study, within the DAM cluster certain type I interferon- and type II interferon-induced genes were inversely correlated, hinting at subtle differences due to local signals. Thus, DAM likely comprise a single population with some heterogeneity. It remains to be seen whether the most dissimilar DAM have consequential differences in function *in vivo*.

While the DAM signature has been best defined using AD and ALS models, it appears in non-neurodegenerative states. Some examples include cuprizone-induced demyelination⁵⁰; aged mice⁴⁷ and the *Ercc1*-deficiency model of DNA damage-accelerated aging⁵¹; and acute facial nucleus degeneration after facial nerve axotomy⁸. The DAM signature is found 16 hours after intracranial injection of apoptotic neurons⁵². Perhaps most surprisingly, a DAM-like population is found in myelin-rich brain regions during the first postnatal week in wild-type mice⁵³. Thus, the DAM state may represent a relatively rapid response to a set of stimuli that happen to accrue in aging and chronic disease and transiently during development. But what might these stimuli be? Tau, SOD1, and axotomy models cause widespread neuron-intrinsic cell death. Cuprizone treatment induces oligodendrocyte death and accumulation of myelin debris. Both aging and development present a combination of apoptotic cells and disordered myelin. DAM may be responding to apoptotic cells specifically; more generally to certain lipidic structures including apoptotic cells but also myelin or protein aggregate-associated apolipoproteins; or even more generally to phagocytosis of any endogenous materials via lysosomal signaling. Either way, the DAM signature seems to be induced by various brain-intrinsic injuries in the absence of massive peripheral infiltrates and can occur on acute to chronic timescales.

TREM2 and downstream targets are required for DAM induction

The pathway that has been most directly linked to DAM activation is the triggering receptor expressed on myeloid cells 2 (TREM2) pathway. Naive TREM2-deficient mice have only very mild differences in microglia transcriptome, morphology, and frequency; however, TREM2-deficient 5XFAD microglia fail to upregulate most DAM genes in response to A β ⁵⁰. On a single-

cell level, very few TREM2-deficient microglia activate to the full extent of wild-type DAM, suggesting that TREM2 deficient cells are inherently limited in activation capacity⁴⁸. A similar dependence of DAM induction on TREM2 was found with cuprizone-induced demyelination⁵⁰, P301S⁵⁴, SOD^{G93A}⁵², and apoptotic neuron injection models⁵². To the contrary, TREM2 deficiency does not block the inflammatory response to endotoxin *in vivo*⁵⁵ and enhances NFκB responses *in vitro*⁵⁶. Thus, TREM2 function seems to be significant specifically in the context of DAM induction. Microglia in kainate-induced acute neurodegeneration⁵⁷ and prion disease⁵⁸ are also affected by TREM2 deficiency, suggesting that these models also induce DAM.

Once the DAM signature has been engaged, certain upregulated molecules may form an autocrine or paracrine loop to sustain it. ApoE is one of the most highly-expressed DAM genes. Total ApoE deficiency reduces the DAM signature in Aβ models^{52,59}, and total knockout or conditional knockout in microglia reduces the DAM signature after acute apoptotic neuron injection⁵², although not as strongly as TREM2 deficiency. These results are consistent with reports that ApoE and clusterin, or ApoJ, are ligands for TREM2⁶⁰⁻⁶², and may hint that ApoE is one of the primary TREM2 ligands in the brain during neurodegeneration. TREM2 is also upregulated in DAM, furthering an ApoE-TREM2 positive feedback loop. Another potential source of positive feedback is CSF-1 upregulation in DAM. This may locally boost CSF1R signaling, which overlaps with and interacts with TREM2 signaling⁶³. The secreted DAM molecule Spp1 is a ligand for the DAM-expressed receptor CD44⁶⁴, representing another potential loop. Another DAM gene that shapes the DAM signature is miR-155⁶⁵, which is upregulated in SOD1^{G93A} microglia dependent on both TREM2 and ApoE and promotes loss of homeostatic microglia gene expression.

1.3 Functions of DAM during neurodegenerative disease

Given the emerging consensus that microglia respond robustly to neurodegenerative disease, much effort has been expended attempting to determine whether microglia are “good” or “bad” in different diseases. Despite some contradictory reports, several mechanisms have been delineated by which microglia can impact disease progression in both positive and negative ways. Because of the conserved nature of the microglia activation signature, it is highly likely that microglia perform similar functions in diverse disease states, with different outcomes depending on the model.

Modulation of pathological protein aggregates

Countless studies have been conducted with amyloid burden as an endpoint in AD models. Increased production of A β is a likely driver of familial forms of early-onset AD^{66,67}. On the other hand, A β accumulation in late-onset AD appears to be driven by decreased clearance of A β . In the PS1-APP mouse model, microglia decreased expression of scavenger receptors (SRs) and A β -degrading proteinases with age⁶⁸. More significantly, metabolic labeling of A β and A β 1-42 in a small cohort of human AD and control subjects revealed that the production to clearance ratio was imbalanced in AD but not control subjects, and this imbalance was driven by a relative decrease in clearance⁶⁹. Mechanisms of microglia-mediated A β clearance have been extensively reviewed, and only select studies will be discussed here⁷⁰⁻⁷². Early studies identified the scavenger receptor CD36 and various TLRs as putative A β receptors on microglia that could direct phagocytosis of fibrillar plaques and demonstrated that deficiency of CD36 increased A β accumulation⁷³⁻⁷⁵.

TREM2 has also been proposed as a receptor for A β /lipoprotein complexes that can directly promote phagocytosis and degradation of A β ⁶⁰, although the effect of modulating TREM2 on A β levels *in vitro* and *in vivo* is not consistent. Interestingly, several studies have called into question whether physiological microglia function leads to a net decrease in amyloid, at least in the setting of commonly used mouse models. In two similar studies, resident microglia were eliminated using genetic ablation systems that resulted in influx of peripherally-derived myeloid cells. These infiltrating cells could partially but not fully recapitulate features of resident microglia. Neither study found a significant effect on A β levels of replacing resident microglia with peripherally-derived microglia^{76,77}. Even near-complete depletion of microglia using a small molecule inhibitor of CSF1R did not alter A β levels in 10-month old 5XFAD mice after a month of treatment⁷⁸. Lower-dose CSF1R inhibition over a longer period of time gave similar results⁷⁹, and one study found that depletion starting from an early age dramatically reduced A β accumulation⁸⁰.

Despite these findings, other reports suggest that microglia have a latent ability to clear A β when inhibitory signals are removed or exogenous activating signals are applied. Viral overexpression of pro-inflammatory cytokines IFN γ , TNF α , or IL-6 could drive microglia proliferation and activation with concomitant A β reduction⁸¹⁻⁸³. Consistent with general microglia activation reducing A β loads, deficiency of the anti-inflammatory cytokine IL-10 decreased A β level while overexpression increased A β level^{84,85}. Several recent translational studies have also highlighted the potential of boosting microglia function as a therapeutic option to reduce A β loads. A promising clinical study demonstrated that monthly systemic administration of the novel anti-A β antibody aducanumab could reduce A β levels in early AD patients, as detected by amyloid PET scan. Parallel experiments in an A β -driven mouse model showed that aducanumab-treated mice had fewer plaques as well as more microglia around plaques, suggesting that the A β reduction

was mediated by microglial Fc receptor engagement of the antibody⁸⁶. A few more exotic therapeutic options have been explored for reducing A β levels via microglia activation. Repeated scanning ultrasound treatments of the brain could reduce A β loads, hypothetically by making microbubbles that disrupt the blood-brain barrier and subsequently change the microglia phenotype. This treatment increased the amount of A β colocalized with microglia lysosomes, suggesting that increased phagocytosis was responsible for the differences⁸⁷. In another unusual approach, A β -bearing mice were optogenetically stimulated in the hippocampus with a 40 Hz signal, within the frequency range that appears most disrupted in AD patients. Stimulation at this frequency altered microglia morphology and increased microglia volume in the hippocampus, which corresponded to increased colocalization of plaques and microglia and decreased overall plaque load. Similar results were obtained in the visual cortex when mice were exposed noninvasively to 40 Hz light flickering⁸⁸. While 40 Hz entrainment signals reduced A β , other frequencies increased A β , so these results should be applied with caution, even if the 40 Hz frequency was chosen *a priori*.

Another way microglia may interact with A β is by forming a barrier around A β plaques that reduces exposure of nearby neurons and astrocytes to soluble and insoluble A β and thereby protects them. Plaque-associated microglia show polarization of phosphotyrosine and microglia receptor staining to the plaque-adjacent surface, and microglia processes cover much of the plaque. In models of deficient plaque-associated microglia such as TREM2 and DAP12 knockout mice, fibrillar A β plaques are looser and have higher surface area by confocal and super-resolution microscopy. Correspondingly, dystrophic neurites are more frequent surrounding these less tightly condensed plaques both in mouse and human AD⁸⁹. A similar phenotype has been observed in ApoE-deficient APPPS1-21 and APP-Swe/PS1-dE9 mice, which also have a diminished DAM

response and decreased microglia localization to plaques. While the total number of fibrillar plaques is dramatically decreased, which is consistent with prior work on ApoE deficiency, the remaining plaques are morphologically less compact, have fewer adjacent microglia, and have correspondingly more surrounding dystrophic neurites on a per-plaque basis⁵⁹. Further experimental manipulations of microglia, such as depletion, are required to pin down whether plaque compaction is a general feature of microglia localization to plaques.

Elimination of synapses and neurons

During development, microglia are essential both for proper pruning of neuronal synapses and for efferocytosis of normally occurring apoptotic neurons. However, both of these functions may go into overdrive during neurodegeneration, leading to excessive loss of neurons and synapses that precipitates or worsens cognitive decline. Synaptic pruning by microglia is dependent on classical complement components⁹⁰⁻⁹² and is modulated by both neuronal activity and CX3CR1-CX3CL1 interaction^{93,94}. In the J20 AD mouse model, this pruning process was shown to be overactive at an early time point preceding plaque deposition and microglia proliferation, with increased presence of complement component C1q and decreased overall numbers of synapses in the hippocampus. Abrogating new production of soluble A β with a γ -secretase inhibitor dramatically decreased the amount of C1q, suggesting that the presence of complement tracks with that of soluble A β . These findings were repeated using an oligomeric A β injection model, and with this system the authors showed that mice deficient in either C1q or the microglia receptor CR3/CD11b did not lose synapses in response to oligomeric A β ⁹⁵.

Complement-dependent loss of synapses has also been reported in various other neuropathological models. Another study observed pronounced synapse loss in CA3 of the hippocampus along with some neuron loss in aged mice compared to young mice. These age-related changes were largely absent in C3-deficient mice. Furthermore, C3-deficient aged mice showed lower anxiety and better learning by behavioral testing than wild-type aged mice⁹⁶. A histological examination of Huntington's disease brain specimens found that complement components are also significantly elevated in this disease relative to control brains, and by in-situ hybridization these components seemed to be produced by microglia, suggesting that a similar phenomenon may occur in Huntington's disease⁹⁷. Clearly, in a variety of settings, activation of the complement cascade can lead to synapse loss. One aspect of this pathway that remains to be clarified is whether increased complement activity on synapses in the diseased state results solely from higher concentrations of complement components overall or also results from increased affinity of synapses for complement. The former is supported by upregulation of complement on the transcriptional level in microglia, and indeed, complement components are prominently expressed in DAM.

Along these lines, microglia activation in general has been linked to heightened neuron loss or cognitive impairment in several studies, although in many cases it is unclear which microglia functions are responsible. Broad inhibition of microglia function can be protective of neuronal function in certain settings. Pharmacological depletion of microglia with a CSF1R antagonist somewhat recovered performance in different behavioral tests in 3xTg and 5XFAD AD mice^{78,79} and decreased neuron and dendritic spine loss in 5XFAD mice. Treatment with the same CSF1R antagonist in a model of cranial irradiation rescued memory deficits associated with irradiation⁹⁸. Analogous results have been obtained with manipulations that do not ablate microglia

but prevent full microglia activation and may represent a specific block of DAM function. In one study, DAP12 deficiency led to recovery of electrophysiological measures and cognitive function in APP/PS1 mice⁹⁹, and TREM2 deficiency dramatically reduced hippocampal atrophy and neuron loss in the P301S model of tauopathy⁵⁴.

In addition to pruning synapses, microglia engulf apoptotic neurons during development via the TAM receptors (Tyro3, Axl, and Mer) that recognize phosphatidylserine directly or indirectly. While Mer is expressed in homeostatic microglia, Axl is upregulated during pathology, including in DAM. In the absence of these receptors apoptotic cells accumulate in the brain. Surprisingly, TAM receptor-deficient mice also accumulate additional live neurons in the olfactory bulb, suggesting that microglia can also engulf certain live neurons with exposed phosphatidylserine, such as stressed neurons. The authors of this study proposed that phagocytosis of stressed neurons could accelerate neurodegeneration, and to support this hypothesis, they demonstrated that mice deficient in both Axl and Mer had a modest increase in survival in the Thy1-Syn^{hA53Tg} model of Parkinson's disease¹⁰⁰. This mechanism has also been supported by live imaging of microglia and neurons in 3xTg mice, which found that microglia tended to colocalize with neurons that subsequently disappeared, hinting that they had been phagocytosed or killed by those microglia. Taken together, an abundance of studies have showed that blocking microglia function during disease can reduce synapse and neuron loss and cognitive decline.

The ability of microglia to exacerbate neurodegeneration was reinforced by several fascinating studies showing spontaneous neurodegeneration attributed to microglia-intrinsic disturbances. These studies demonstrate that microglia overactivity is sufficient to cause neurodegeneration. Microglia deficiency of NRROS, a gene that is thought to negatively regulate

ROS production, leads to loss of the homeostatic microglia signature, including the master regulator Sall1. In NRROS-deficient mice, the predominant myeloid cells in the brain instead express many markers of perivascular macrophages. Temporally controlled conditional knockout experiments established that NRROS is required during development and its absence leads to sustained alterations in microglia identity. Starting at around 3-4 months of age, these mice develop a progressive, lethal neurodegenerative disease with motor deficits¹⁰¹. In a completely different system, constitutive activation of the MAPK pathway in microglia was established by inducible expression of constitutively active Braf V600E. This manipulation causes microglia proliferation and activation in various regions of the brain and, as with NRROS deficiency, leads to a neurodegenerative phenotype characterized by synapse and neuron loss, motor deficits, and death with approximately the same time course¹⁰². Finally, a model of CNS TGF β deficiency that disrupts the homeostatic microglia signature also led to motor deficits starting, once again, at around 4 months of age¹⁸. However, this particular result is confounded by presumably decreased TGF β signaling in neurons, which is important for neuron survival¹⁰³; in addition, microglia were relatively depleted, even though remaining microglia did lack the homeostatic microglia signature and appeared more activated. Other examples of microglia activation possibly being sufficient to cause neurodegeneration are the interferonopathies discussed in the previous section. Thus, microglia strongly activated in certain ways can initiate neuron loss and neurodegeneration without other pathological inputs.

1.4 Genetic implication of microglia in neurodegeneration

Rare neurological diseases driven by loss of microglia

The most striking genetic implication of microglia in neurodegenerative disease was the identification of homozygous loss-of-function mutations in TREM2, or its required adaptor for trafficking and signaling DAP12, as the cause of Nasu-Hakola disease^{104,105}. This condition is an extremely rare, lethal autosomal recessive disease involving formation of bone cysts and then neurodegeneration of white matter that resembles frontotemporal dementia beginning in middle age¹⁰⁶. While DAP12 is expressed in a variety of innate immune cells, TREM2 is exclusive to the myeloid lineage, and within the brain, to microglia. Thus, a microglia-specific defect can drive early-onset neurodegenerative disease. Impaired clearance of myelin debris was observed in TREM2-deficient mice fed the demyelinating compound cuprizone, partially reproducing the pathology in mice^{50,107}. A similar neurodegenerative phenotype also featuring white matter dysfunction, known as hereditary diffuse leukoencephalopathy, is found in patients carrying rare heterozygous loss of function mutations in the essential myeloid lineage growth factor receptor CSF1R^{108–110}, pointing to a common mechanism. Indeed, CSF1R and DAP12 have been reported to signal via common downstream pathways⁶³. However, one key difference is that at least in mouse models, TREM2/DAP12 signaling are not essential for microglia survival in young adult mice and TREM2-deficient brains do not show obvious histological differences, whereas CSF1R-deficient mice lack microglia and have other brain abnormalities^{111,112}. With TREM2/DAP12 deficiency, functional differences only manifest during disease or aging and are associated with impaired microglia activation as opposed to resting microglia function. Thus, it is possible that in Nasu-Hakola disease, a specific loss of DAM leads to the neurodegenerative phenotype.

Alzheimer's disease

Despite these findings, microglia did not feature in mainstream theories of sporadic forms of neurodegeneration until recently. The past decade has seen a dramatic shift in the estimation of the immune component of AD, in particular. Large-scale human studies have revealed a multitude of microglia-enriched loci and pathways linked to AD, and unbiased bioinformatics studies have implicated the microglia response as the strongest transcriptional signal in AD pathogenesis by different approaches²⁷. Utilizing human brain transcriptomic data to construct gene interaction networks revealed changes in immune genes in human AD²⁸ and specifically modules centered on *TREM2*¹¹³. Epigenetic analysis of a mouse model of AD and human data found widespread changes in genes regulated by PU.1, a master transcription factor for microglia and other myeloid cells¹¹⁴. Most of these studies are correlative and performed on whole tissue, so they principally indicate that microglia proliferate and change during AD, without necessarily allowing causal inferences to be made.

The first hints of a causal, genetic link between microglia and AD were the identification of common variants in immune system-specific genes *CRI*¹¹⁵, *CD33*¹¹⁶, and *INPP5D*¹¹⁷ that had very modest effects on AD risk, on the scale of 5-10% differences in odds ratio. *CD33* deficiency has been studied in a mouse model of AD, showing effects on A β that mirror the effects of AD risk¹¹⁸. These exciting findings lent support to a role for microglia in AD as modifiers of disease and not just bystanders, but the small effect sizes suggested that microglia were not central players. Much more revealing from a pathogenetic standpoint was the discovery of a several-fold increase in AD risk associated with the rare R47H allele of *TREM2*^{119,120}. This discovery was even more striking because of the previously known link between *TREM2* and Nasu-Hakola disease.

Subsequent studies of R47H and AD risk confirmed a strong association, although with variable odds ratios^{121–126}. In addition to R47H, other *TREM2* variants have been investigated in relation to AD risk. The R62H variant occurs relatively frequently in Caucasian populations and substantially increases AD risk, albeit less than R47H^{123,124}. Among African Americans, the tightly linked T96K and L211P variants are fairly common and lead to a moderate increase in AD risk of around 25%¹²⁷. The R47H variant is extremely rare in the Japanese¹²⁸ and Han Chinese¹²⁹ populations; however, the H157Y variant did increase AD risk by several fold in a Han Chinese cohort, on a similar scale as R47H¹³⁰.

Other significant risk alleles for AD and other neurodegenerative diseases occur in genes that are not conventionally thought of as microglia genes but which may nonetheless exert their effects partially through microglia. The *APOE* ϵ 4 risk allele, which makes the greatest single-locus contribution to genetic risk for late-onset AD^{131,132}, appears to boost microglia activation and worsen pathology in a P301S tauopathy mouse model. At least some of the neurotoxic effects of ApoE ϵ 4 could be reproduced *in vitro* with microglia-specific modulation of ApoE isoform. The authors hypothesized that ApoE ϵ 4 drives microglia activation and the AD risk associated with ApoE ϵ 4 could be partially through effects on microglia and further downstream, through neurotoxic astrocytes¹³³. However, they could not definitively demonstrate that this deleterious effect of ApoE ϵ 4 requires microglia using *in vivo* microglia-specific manipulations; given the widespread effects of ApoE on different CNS cell types, an alternative explanation is that the increased neurodegeneration caused by ApoE ϵ 4 independent of microglia secondarily boosts microglia activation. Another gene linked to AD risk is clusterin¹¹⁵, or ApoJ, which was recently shown to be a ligand for *TREM2* and may have similar effects as ApoE on microglia.

Other neurodegenerative diseases

In other neurodegenerative diseases caused by known pathogenic mutations, some evidence also points to primary microglia involvement. Mutations in *SOD1* have long been known to drive a small subset of familial ALS cases¹³⁴. Based on the normal function of SOD1 in generating ROS, which could be neurotoxic, a role for microglia was suspected; however, the discovery of motoneuron aggregates of mutant SOD1 proteins and a lack of dependence of the phenotype on endogenous SOD1 made a strong case that the mutant forms cause motoneuron-intrinsic cell death¹³⁵. However, overexpression of mutant SOD1 exclusively in motoneurons¹³⁶ or even all neurons¹³⁷ was not sufficient to drive loss of motoneurons and motor deficits. Furthermore, deletion of mutant SOD1 from either neurons or microglia could extend lifespan in mice¹³⁸, as could transplantation of mutant SOD1 mice with wild-type bone marrow¹³⁹, suggesting that the expression of SOD1 in microglia somehow affects disease. Notably, the mechanism for microglia involvement in this form of ALS may be entirely different from the typical DAM response; indeed, microglia numbers and morphology appeared to be similar between microglia-deleted and non-microglia-deleted mutant SOD1 mice. A very limited clinical trial of bone marrow transplantation for sporadic ALS did not have any clinical benefit despite successful engraftment of some patients¹⁴⁰, but sporadic ALS is likely to be fundamentally different from mutant SOD1-driven ALS. A recently appreciated driver of familial autosomal dominant ALS and FTD is intronic repeat expansions in *C9orf72*. While many studies have now discovered dramatic gain-of-function toxic effects of these repeats both from the transcribed RNA as well as from the unconventionally translated dipeptide repeats^{141–147}, and these effects appear to be sufficient to cause neurodegeneration, the repeats also lead to decreased *C9orf72* expression. A study of *C9orf72*-deficient mice found that while there was no overt neurodegeneration due to *C9orf72*

deficiency, aged mice had severe immune dysregulation that was traced to macrophage and microglia function. Without *C9orf72*, macrophages accumulate lysosomes and have altered inflammatory responses¹⁴⁸. Overall, the clearest sources of pathogenicity with *C9orf72* repeat expansion are neuron-intrinsic, and the effects of *C9orf72* deficiency are not seen in heterozygous mice, which would be analogous to human disease. Still, hampered microglia function might have a minor contribution for this form of ALS/FTD. Another genetic analysis found that rare loss of function mutations in *TBK1*, a gene that is important for interferon production as well as autophagy, could cause familial ALS/FTD. The clear role of *TBK1* in immune function is interesting, but this study found that several of the implicated mutations impact binding of *TBK1* to optineurin but not phosphorylation of targets associated with interferon production¹⁴⁹. Thus, these mutations may affect neuronal pathways independent of microglia or inflammation.

Other neurodegenerative diseases have less clear genetic evidence for microglia involvement. While an expression quantitative trait locus for *MHCII* has been linked to a 15-30% increased risk for sporadic Parkinson's disease, which suggests that adaptive immunity may have a role in the disease, other early-onset and sporadic Parkinson's disease polymorphisms are not clearly linked to microglia^{150,151}. Huntington's disease, as with certain familial forms of AD, ALS/FTD, and Parkinson's disease, has a clear cause: autosomal dominant repeat expansions in the huntingtin protein¹⁵². These repeats are known to lead to abnormal RNA and protein species that can interfere with cellular function¹⁵³. Huntingtin is expressed in various cell types in the brain and could theoretically act in microglia. While neuron-intrinsic cell death through these mechanisms is a simple and appealing model for the neuron loss seen in Huntington's disease, a few studies have hinted at neuron-extrinsic mechanisms. Peripheral blood from mutant huntingtin carriers had abnormal inflammatory signatures well before predicted disease onset. Inflammatory

cytokines, especially IL-6, were elevated in plasma of these premanifest individuals, and their peripheral blood monocytes produced more cytokines in response to LPS + IFN γ stimulation. Microglia and macrophages from several mutant huntingtin-expressing mouse models had a similarly exaggerated inflammatory response¹⁵⁴. These findings were strengthened by a later study using novel cell lines and mouse models. In the BV2 myeloid cell line, in which mutant huntingtin expression increased expression of the key myeloid lineage factors PU.1 and C/EBP and target genes IRF1 and TLR2, in addition to IL-6 and TNF α . Direct binding of these transcription factors to target gene loci was confirmed by chromatin immunoprecipitation, and the upregulation of these genes was confirmed in primary microglia from mutant huntingtin-expressing mice as well as brain specimens from Huntington's disease patients. The most significant finding was that in mice that conditionally express mutant huntingtin in CX3CR1-positive microglia, expression of these same genes was elevated. Mutant huntingtin-expressing microglia promoted neuron death in a co-culture system as well as in their microglia-specific mouse model *in vivo* in the presence of LPS¹⁵⁵. Therefore, in Huntington's disease, as in SOD1-linked ALS, expression of the mutant protein in microglia could be causing microglia dysregulation that causes or contributes to disease.

1.5 Rationale for TREM2 study

The many confounds and ambiguity that arise when interpreting the effect on microglia of the mutations just described have led to increased attention being paid to the R47H TREM2 variant. Due to specific expression of TREM2 in microglia, the linkage between TREM2 mutation and disease is mechanistically constrained to microglia-dependent processes. Overall, the most clearly microglia-related pathogenic mutations in TREM2/DAP12 and CSF1R all seem to reduce

microglia function while promoting neurodegenerative disease, whereas other pathogenic mutations may affect microglia but not necessarily in a cell-intrinsic way, making them harder to interpret. To better understand whether microglia are beneficial or harmful for AD, many investigators have seized on the TREM2 lead and attempted to answer two essential questions: what is the effect of TREM2 variants on TREM2, and what is the effect of TREM2 on microglia? This thesis also broadly adopts this approach. Chapter 2 examines the *in vitro* and *in vivo* effects of AD-associated TREM2 variants and is largely adapted from two studies published as a result of this work^{156,157}. Chapter 3 examines the mechanism by which TREM2 acts in microglia, and is derived partially from an additional study published as a result of this work¹⁵⁸. As TREM2 variants modify AD risk in heterozygosity and gene dose-dependent effects are also observed in mouse models, regulation of TREM2 expression likely plays an important role in disease progression. Thus, Chapter 4 will describe an unbiased screen for genes that regulate TREM2 surface levels. A better understanding of the basic biology of TREM2 regulation, function in microglia, and effect of mutations will pave the road for future therapeutic efforts. This introductory chapter (Chapter 1) was derived in part from a review written as part of this thesis¹⁵⁹.

Chapter 2: Impact of TREM2 variants on

TREM2 function *in vitro* and *in vivo*

Given the strong, consistent association of R47H with increased AD risk, and the identification of additional variants with weaker associations with AD, whether and how these variants affect TREM2 function is of utmost importance to understand and target TREM2 in AD. If risk is associated with loss of function, this would favor TREM2-enhancing therapies, whereas if risk is associated with gain of function, this would favor TREM2-inhibiting therapies. Correlating genetic risk with functional impact *in vitro* can help to address this question, an approach taken in the first part of this chapter. Regarding the best-established R47H variant, *in vitro* experiments and study of cross-sectional human specimens have suggested the R47H variant decreases TREM2 function, but both approaches have caveats. *In vitro* studies may not pinpoint a physiologically relevant readout. On the other hand, AD cases partially driven by microglia dysfunction may have a different natural history than other sporadic cases, complicating cross-sectional analysis. A mouse model of AD can strictly control timing and genetic background to isolate the effect of the variant. In addition, the human and mouse genes only share about 77% sequence identity, meaning that non-conserved regions could potentially modulate the repertoire of ligands, overall binding affinity, and the effects of variants. To address both issues, we generated two mouse lines with either common variant (CV) or R47H human TREM2 (hTREM2) in place of murine TREM2 (mTREM2) in the 5XFAD AD mouse model to investigate the effect of the R47H variant in a controlled *in vivo* setting.

2.1 *In vitro* characterization of TREM2 variants

We generated a retroviral construct overexpressing human TREM2 and human DAP12 under control of the CMV promotor and separated by an internal ribosomal entry sequence (IRES). This construct was used to generate the corresponding point mutations by site-directed mutagenesis. Once the panel of constructs was obtained, we packaged retroviral particles by transfecting 293T cells with equal amounts of construct DNA and harvesting viral particles in parallel. To assay TREM2 signaling, we started with the 2B4 NFAT-GFP cell line, which is a T cell hybridoma that expresses EGFP in response to calcium signaling. After transducing TREM2/DAP12 into these cells, we sorted transduced cells by two rounds of fluorescence-activated cell sorting (FACS) for TREM2 expression to select stable expressers. The common variant of TREM2 (TREM2-CV) and non-transduced reporter cells served as positive and negative controls, respectively. By flow cytometry, surface expression ranged from about 50% to 120% of TREM2-CV (**Fig. 1A**). The T66M variant had no detectable surface expression, as previously shown, and did not show any activation in our assay (data not shown). On the other hand, the R52H, R62C, and T96K mutations demonstrated somewhat lower surface expression despite their higher RNA expression, which may reflect a true defect in protein trafficking or simply technical variation. Using these reporter lines, we analyzed TREM2 activation in response to a variety of known lipid ligands. Each ligand was coated on a 96-well plate at different concentrations, and reporter cells containing each TREM2 variant were subsequently plated in duplicate. After 12 hours, the percentage of GFP⁺ cells at each concentration was determined by flow cytometry. Then, the baseline activation with no ligand was subtracted from each respective activation curve and area under the curve (AUC) relative to TREM2-CV was used to compare overall activation. An example of a full activation curve is shown in **Fig. 1B**.

Because of the correlation between surface expression and activation seen with antibody stimulation, we used the activation/expression ratio to determine functional impact. **Fig. 1C** shows activation versus surface expression plots for the purified lipid ligands phosphatidylserine (PS), sulfatide (Sulf), and phosphatidylcholine (PC). As lipoproteins contain a variety of phospholipids, we tested whether abundant serum lipoproteins such as high density lipoprotein (HDL) and low-density lipoprotein (LDL) could activate TREM2 in our reporter system. Indeed, both HDL and LDL activated TREM2 variants in a similar pattern as seen for purified phospholipids (**Fig. 1D**). These results extend the range of TREM2 ligands and are consistent with the recent observation that lipoprotein particles containing the apolipoprotein E (ApoE) also bind TREM2^{61,62}, which is notable given the association of ApoE polymorphisms with AD.

As previously shown⁴⁰, the R47H polymorphism has a profound negative impact on signaling in response to all tested ligands except PC, which in turn elicited a normal response from all variants. The R62C polymorphism showed a similarly dramatic reduction in activation. The H157Y and R62H variants demonstrated a lesser defect. To the contrary, T96K and D87N had consistently higher activation. R52H, R136W, L211P, and E151K were neutral overall. The percentage deviations of each variant from TREM2-CV across ligands are summarized in **Fig. 1E**. As Q33X leads to truncation of nearly the entire protein, it presumably leads to complete loss of function and thus was not assayed.

To correlate these variants to human genetics, we analyzed data on these variants in the NIMH AD Genetics Initiative Study and AD Sequencing Project (**Table 1**). Family-based association analysis (FBAT) in the NIMH AD families yielded a p-value of 0.004 for R47H, consistent with our previous report in the same NIMH families (11) and confirmed in ADSP ($p < 3.45e-12$; OR=4.5). Other rare variants in TREM2 were not present in more than ten

statistically informative families, thereby preventing the computation of reliable p-values. However, several variants were frequent enough to be suggestive between both datasets. R62H had an odds ratio (OR) of 1.7 in NIMH families, confirmed in ADSP (p=0.006; OR=1.4). The related R62C was found in two affected individuals from one NIMH family and had an OR of 0.58 in ADSP, but numbers were too small to draw conclusions. T96K and L211P, which were almost completely linked in both datasets, had OR around 10 in NIMH families, but this was not supported by the replication sample (p=0.85; OR=1.04; p=0.59; OR=1.13, respectively). On the other hand, D87N had an OR of 0.89 in NIMH families but was significantly associated with risk in ADSP (p=0.017; OR=2.3). Both of these variants showed conflicted results in other cohorts, so their contribution to AD risk is still questionable. The stop gain Q33X was biased toward affected individuals in NIMH families and statistically significant for increased risk in ADSP (p=0.025). Finally, H157Y was found in 5/8 affected individuals, but no unaffected individuals were available for comparison; however, it significantly increased risk in ADSP (p=0.01; OR=4.7), and additional studies have replicated this risk. Overall, in addition to R47H, which already had strong evidence for increased AD risk and decreased *in vitro* function, we provide evidence that R62H, H157Y, and Q33X also show this same correlation. On the other hand, D87N and T96K/L211P showed dramatic gain-of-function effects in our assay but the genetics is not established conclusively.

2.2 *In vivo* characterization of R47H variant

To understand the *in vivo* properties of hTREM2 and the R47H polymorphism, we generated several BAC transgenic lines expressing either the common hTREM2 variant (CV) or

the R47H polymorphism (R47H). A BAC clone was selected that contained abundant flanking sequence of the TREM2 gene to allow endogenous expression of TREM2. We first assessed cell surface expression of hTREM2 in each of these lines to ensure that both CV and R47H transgenic mice generated using this strategy express hTREM2 on the cell surface in a pattern paralleling that of murine TREM2, i.e. on myeloid cell populations previously shown to express TREM2. We selected two lines - one carrying CV and one carrying R47H - that expressed similar levels of hTREM2 on the cell surface. Thioglycolate-elicited peritoneal macrophages were collected on day 3 post-injection and stained for hTREM2, revealing expression of both transgenes at similar levels in these lines (**Fig. 2A**). Bone marrow-derived macrophages (BMDMs) were stained for hTREM2 after 2 days of culture, showing hTREM2 specifically on F4/80⁺ differentiated cells, again at similar levels in both transgenic lines (**Fig. 2B**). hTREM2 mRNA in the cortex was quantified by qPCR, revealing slightly lower mRNA in R47H compared to CV brains (**Fig. 2C**). However, quantification of hTREM2 protein in the brain by immunoblotting the PBS-insoluble fraction of hippocampal homogenates (including membrane-bound protein) showed similar levels between transgenic lines on the protein level (**Fig. 2D**). These mice were bred with *mTREM2*^{-/-} (KO) mice to obtain CV and R47H transgenic mice lacking endogenous TREM2. Next, we crossed CV and R47H to 5XFAD mice, in which amyloid pathology is driven by overexpression of mutant human APP and PS1, and compared these CV⁺ *mTREM2*^{-/-} 5XFAD (CV-KO-5x5XFAD) and R47H⁺ *mTREM2*^{-/-} 5XFAD (R47H-KO-5XFAD) mice to *mTREM2*^{-/-} 5XFAD (KO-5XFAD) mice at 8 months of age. hTREM2 was visualized by immunofluorescence microscopy in steady-state microglia but not in other CNS cells (**Fig. 2E**). Quantification of staining intensity showed that microglia had similar hTREM2

levels between transgenic lines on a per-voxel basis, and staining intensity increased in 5XFAD brains (**Fig. 2F**).

To understand the effect of CV and R47H on microglia, we started by examining microglial numbers throughout the cortex and hippocampus (**Fig. 3A**), as well as specifically adjacent to plaques (**Fig. 3B**). By both measures, microglial numbers were enhanced by both CV and R47H transgenes compared to KO, with CV having a larger effect. Since microglia clustering around plaques has been proposed to promote A β clearance, we also measured A β levels by both imaging and ELISA. Total fibrillar plaque area in the cortex, subiculum, and hippocampus (excluding subiculum) was determined by manual selection of the relevant regions followed by automated determination of threshold and calculation of percent area covered (**Fig. 4A**). As a complementary measurement, flash-frozen cortical tissue was homogenized sequentially in PBS and guanidine solutions to obtain PBS-soluble and -insoluble fractions. A β ₁₋₄₀ and A β ₁₋₄₂ levels were measured in both fractions by ELISA in the hippocampus (**Fig. 4B**) and cortex (**Fig. 4C**). By either modality, A β was generally unaltered by CV and R47H, excepting a slightly decrease in hippocampal PBS-soluble A β species. Thus, while R47H affects microgliosis, the decreased number of microglia in R47H-KO-5XFAD compared to CV-KO-5XFAD was not sufficient to affect plaque coverage, or to cause a detectable difference in accumulation of A β plaques in our model.

To more clearly understand the microglia-intrinsic effect of the R47H variant, we performed qRT-PCR analysis of whole cortex for microglia activation-related transcripts. The microglia-specific genes *Spp1*, *Gpnmb*, and *Cst7*, encoding osteopontin, osteoactivin, and cystatin F, respectively, are among the most upregulated in AD models^{39,40}. All three activation

markers were much more upregulated in CV-KO-5XFAD than in other genotypes, suggesting that the R47H variants exhibit a defect in promoting microglia activation (**Fig. 5A**).

To acquire a global snapshot of transcriptional differences between microglia in different conditions, we performed microarray analysis of sorted microglia from brains of 8.5-month-old 5XFAD animals. A gene list of microglial activation markers was compiled from our previous data using the same platform by selecting genes upregulated at least 2-fold between 5XFAD and non-5XFAD microglia and ordering them based on their upregulation in TREM2-deficient microglia. Genes that were more highly upregulated in TREM2-sufficient compared to TREM2-deficient microglia were deemed TREM2-dependent, and genes with similar upregulation were deemed TREM2-independent. Unsupervised clustering of samples based on this microglia activation signature grouped KO-5XFAD and R47H-KO-5XFAD together, distinct from CV-KO-5XFAD, and revealed a stepwise increase in activation from KO-5XFAD to R47H-KO-5XFAD to CV-KO-5XFAD (**Fig. 5B**). Furthermore, differences between the groups were more pronounced among TREM2-dependent than TREM2-independent genes. We verified that *Spp1* was upregulated on the protein level in a TREM2-dependent manner by confocal microscopy (**Fig. 5C**). A large proportion of CV-KO-5XFAD microglia in cortex and hippocampus were positive for *Spp1* staining, whereas few positive microglia were observed in R47H-KO-5XFAD and virtually none in KO-5XFAD (**Fig. 5D**). We conclude that CV mediates activation of microglia, which is partially affected by R47H, and *Spp1* is a sensitive marker of TREM2-dependent activation on the mRNA and protein level.

Given recent studies on TREM2 polarization during A β accumulation, we sought to shed light on localization of CV and R47H hTREM2. While hTREM2 is exclusively detected in Iba-1+ microglia using an antibody directed against its intracellular C-terminus (**Fig. 2**), brain

sections stained with an antibody against hTREM2 extracellular domain (ECD) showed diffuse distribution of hTREM2 outside of Iba-1+ voxels (**Fig. 6A**) and hTREM2 C-terminus+ voxels in CV-KO-5XFAD mice (**Fig. 6B**), suggesting the presence of soluble TREM2. The intensity of hTREM2 ECD staining was quantified both within Iba-1+ voxels and within Iba-1- voxels in the cortex (**Fig. 6C**) and hippocampus (**Fig. 6D**). While hTREM2 ECD intensity within microglia remained relatively constant between non-5XFAD and 5XFAD images, hTREM2 intensity outside microglia dramatically increased in CV-KO-5XFAD images and slightly increased in R47H-KO-5XFAD images. This non-microglial staining was absent in KO-5XFAD.

A particularly intense hTREM2 ECD staining was observed on a fraction of non-microglial cells and A β plaques. Co-staining for NeuN and hTREM2 ECD demonstrated that the hTREM2 ECD+ cells are neurons (**Fig. 6E**). Quantification of hTREM2 intensity specifically in NeuN+ neuronal soma showed that CV-KO-5XFAD mice had higher frequency of hTREM2+ neurons (**Fig. 6F**) and higher hTREM2 intensity in neuronal soma (**Fig. 6G**) than R47H-KO-5XFAD mice in both cortex and hippocampus. Similarly, hTREM2 intensity in A β plaques was higher in CV-KO-5XFAD mice than R47H-KO-5XFAD mice in both cortex and hippocampus (**Fig. 6H**). While TREM2 has been reported to bind damage-associated phospholipids such as phosphatidylserine, hTREM2 ECD did not colocalize to APP+ dystrophic neurites (**Fig. 6I**), and nuclei of hTREM2+ neurons did not show morphological abnormalities such as pyknosis or fragmentation (**Fig. 6J**). To verify that the unique distribution of hTREM2 ECD reflected soluble TREM2, we performed immunoblots on the PBS-soluble fraction of hippocampal tissue homogenates for TREM2 (**Fig. 6K**). A low molecular weight hTREM2 smear was detected, with the lower range of the smear corresponding to the predicted soluble hTREM2 size of 20 kDa. Densitometry confirmed higher soluble TREM2 levels in CV-KO-5XFAD compared to R47H-

KO-5XFAD. Overall our results show for the first time that soluble TREM2 production markedly increases during A β accumulation in a mouse model and associates directly with neurons and plaques in vivo. The increase of soluble TREM2 and its broad distribution are both impaired by the R47H variant.

We sought to shed light on the differences in soluble TREM2 observed between genotypes. To that end, we generated RAW264.7 macrophage-like cell lines that overexpress either CV or R47H. Previous work had indicated that diverse immunostimulatory molecules such as LPS, TNF α , and IFN γ could lead to downregulation of cell-surface TREM2. We found that in our system, surface expression of both CV and R47H, as measured by flow cytometry, could indeed be downregulated by these molecules within two hours of stimulation (**Fig. 7A**). While LPS and TNF α led to a rapid down-regulation of surface hTREM2 at 30 minutes and partial recovery by 2 hours, IFN γ had no detectable effect at 30 minutes but decreased surface hTREM2 by 2 hours. To determine whether these changes were due to cleavage, we lentivirally transduced cells with Cas9 and a guide RNA against Adam17, which was previously shown to cleave TREM2. Unlike non-transduced cells, a fraction of transduced cells retained TREM2 surface expression upon LPS treatment (**Fig. 7B**); this seemingly cleavage-resistant fraction (+) was purified from the remainder of cleavage-sensitive transduced cells (-) by fluorescence-activated cell sorting and both populations were analyzed by immunoblot for Adam17 protein levels (**Fig. 7C**). The (-) population showed only a slight decrease in Adam17 protein relative to non-transduced cells, possibly reflecting the presence of heterozygous Adam17 knockout, whereas the (+) population showed virtually no residual Adam17 expression and were considered Adam17 KO. LPS, TNF α , and IFN γ treatment all failed to decrease TREM2 surface expression in CV-Adam17 KO and R47H-Adam17 KO (**Fig. 7D**). These results suggest that various

myeloid cell signaling pathways that may be activated in neuropathology can induce Adam17-dependent release of soluble TREM2 and that R47H polymorphism does not directly impact this process.

Our study provides conclusive evidence that the R47H polymorphism reduces TREM2-dependent phenotypes in microglia *in vivo*, in the setting of endogenous ligands of TREM2 in the mouse brain. Compared to CV-expressing brains, R47H-expressing brains had decreased microglia numbers, slightly increased soluble A β , and dramatic reductions in activation markers and soluble TREM2. We further suggest that soluble TREM2 differences between the two lines are due to differences in microglial activation rather than intrinsic differences in cleavability between CV and R47H TREM2. Future studies should examine some of the other established TREM2 variants, such as R62H or H157Y, *in vivo*. More importantly, better powered genetic data on rare TREM2 variants such as D87N and T96K/L211P, along with additional functional studies, will help to clarify whether TREM2 gain-of-function is detrimental in AD.

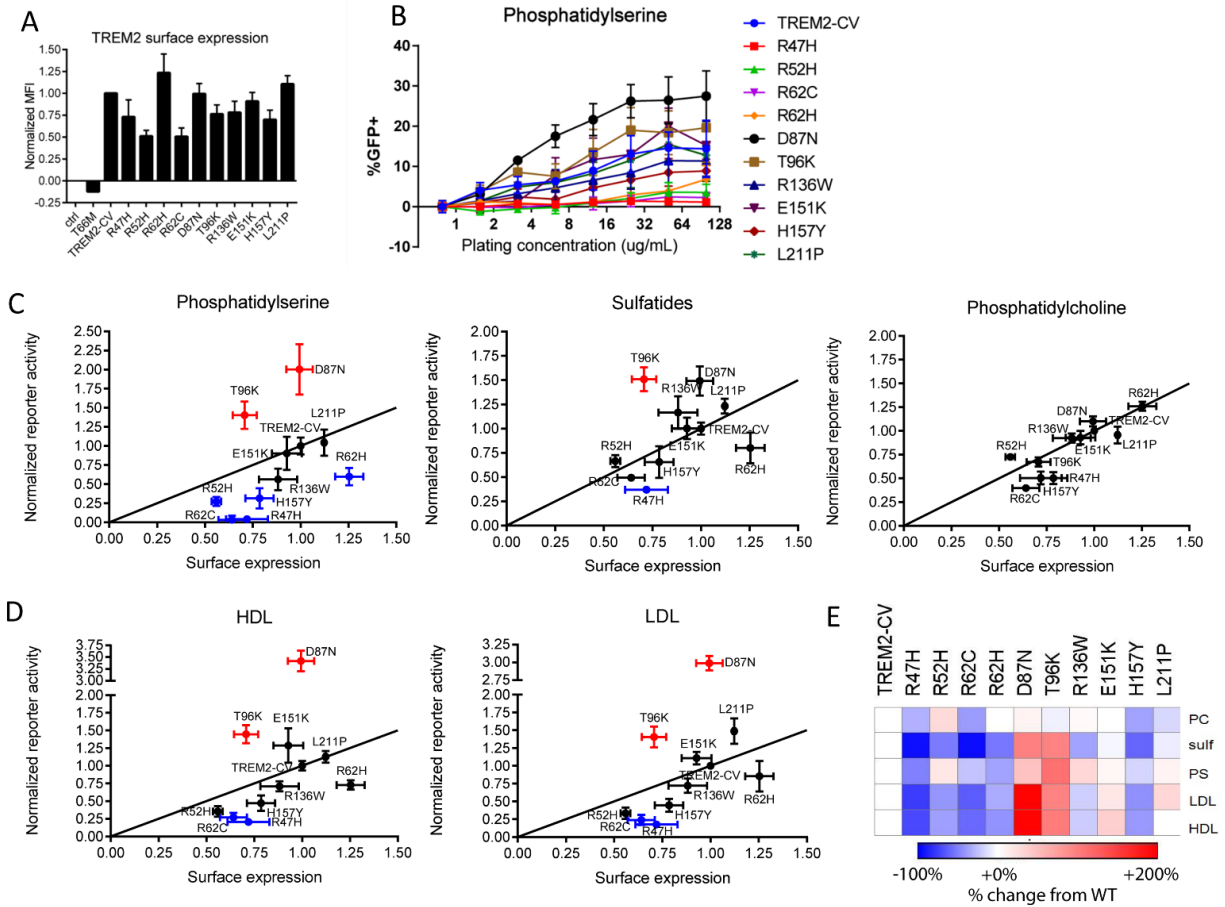


Figure 1. TREM2 variants affect ligand binding in a reporter cell assay.

A panel of TREM2 variant-expressing reporter cells were generated by retroviral TREM2 overexpression and sorted for TREM2 surface expression. **(A)** TREM2 gMFI of different variants compared to common variant (CV). **(B)** Activation of different reporter lines in response to different concentrations of plate-coated phosphatidylserine. **(C)** Activation AUC vs. surface expression of different variants in response to phosphatidylserine, sulfatides, and phosphatidylcholine. Black line represents a relative activation/surface expression ratio of 1 compared to CV. Red points are significantly higher than CV, while blue points are significantly lower. **(D)** Similar plots as **(C)** for plate-coated HDL and LDL. **(E)** Summary of variants for different ligands compared to CV.

Table 1. TREM2 gene variants found in the NIMH family-based WGS data and tested for replication in the ADSP case-control samples.

Codon change	#Families	#Aff Carr	Med. AAO	#Unaff Carr	Med. Age	MAF	OR	NIMH (P-val)	ADSP-WES MAF	P-val; OR(CI);
R62C	1	2/2	78	0/0	--	0.00068	NA	--	0.65; 0.58(0.05~6.43);	0.0001
Q33*	2	4/4	71	1/3	73	0.00170	NA	--	0.025; (NA);	0.0001
R47H	20	35/53	72.5	2/14	72	0.01390	11.7	0.004	3.45E-12; 4.5(2.7~7.4);	0.005
T96K	9	11/16	71	1/6	79	0.00475	11	--	0.85; 1.04(0.65~1.67);	0.003
R62H	11	12/23	73	7/18	72	0.00746	1.7	--	0.006; 1.44(1.1~1.88);	0.01
H157Y	4	5/8	74	0/0	--	0.00203	NA	--	0.01; 4.7(1.04~21.33);	0.0006
L211P	10	12/18	71	1/6	79	0.00509	10	--	0.59; 1.13(0.71~1.81);	0.003
D87N	5	4/13	76	2/6	76	0.002	0.89	--	0.017; 2.3(1.1~5.1);	0.0015

#Aff Carr: affected carriers over total affected subjects. Med. AAO: median age of onset in affected carriers. #Unaff Carr: unaffected carriers over total unaffected subjects. Med. Age: median of last known ages of the unaffected carriers. MAF: minor allele frequency. CI: confidence interval.

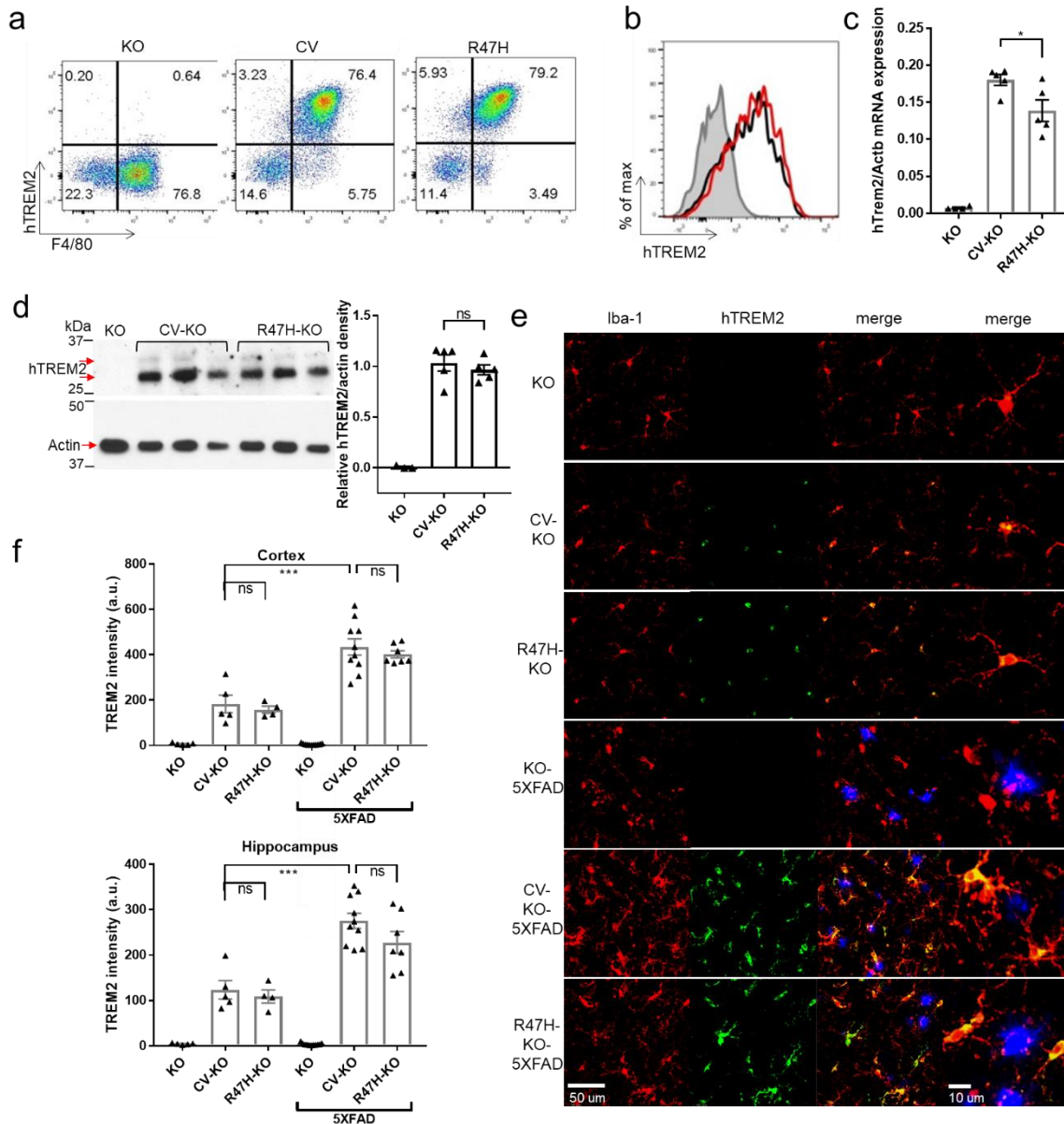
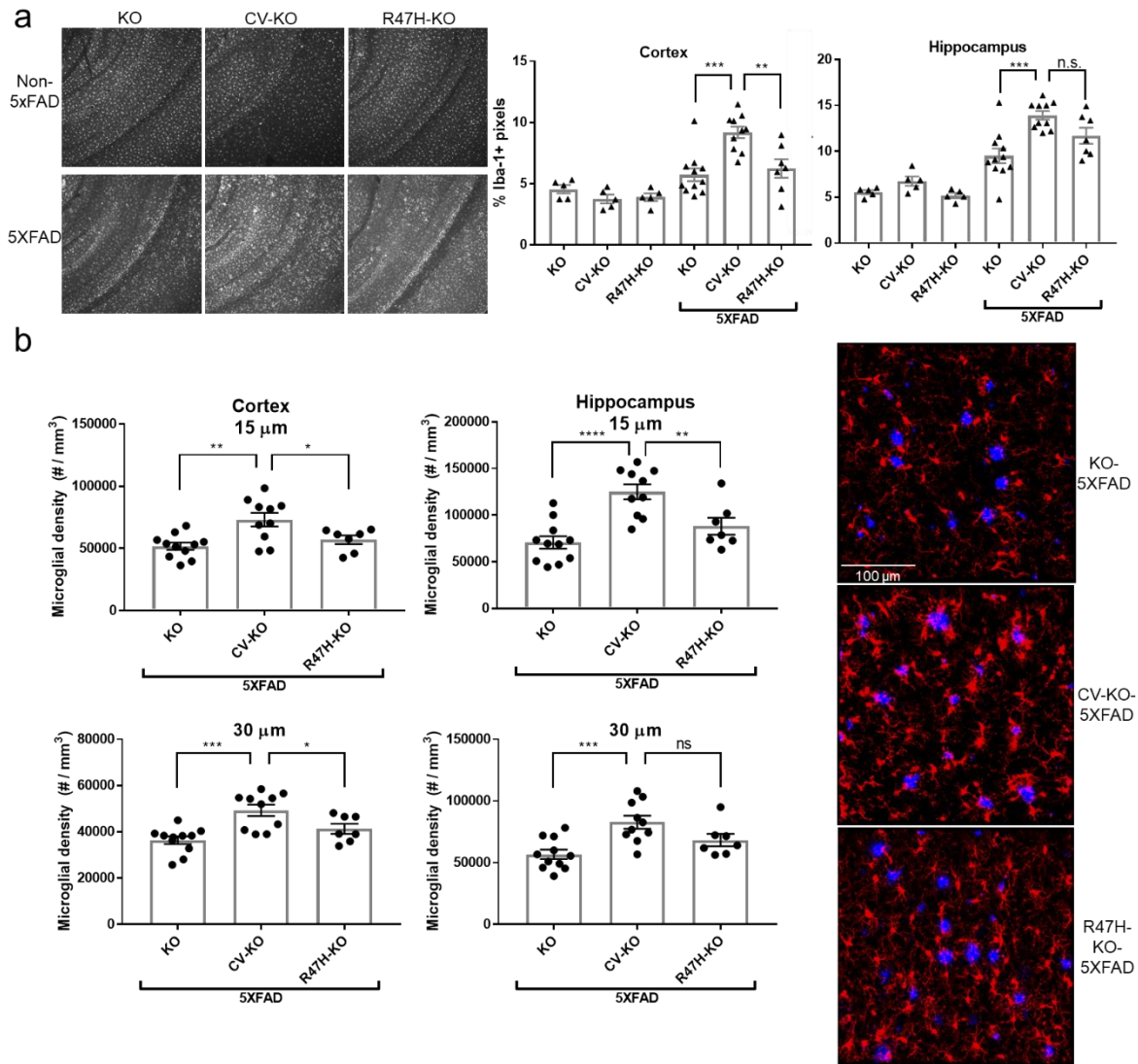


Figure 2. CV and R47H transgenes are specifically expressed in myeloid cell populations at comparable levels.

(A) Thioglycolate-elicited peritoneal macrophages were stained for macrophage marker F4/80 and hTREM2, showing similar level of hTREM2 in F4/80⁺ cells from both CV and R47H mice. (B) Bone marrow-derived macrophages were stained after 2 days in culture and gated on CD11b⁺ cells. (C) hTREM2 mRNA expression in KO, CV-KO and R47H-KO whole cortical tissue. (D) Immunoblot of hTREM2 and actin in the PBS-insoluble fraction of hippocampal tissue homogenates. (E) Confocal microscopy of cortex of CV-KO, R47H-KO, or KO 5XFAD or non-5XFAD mice shows colocalization of hTREM2 C-terminus (green) and microglial marker Iba-1 (red); methoxy-X04 staining for plaques is shown in blue. (F) Quantification of staining intensity of hTREM2 in the cortex and hippocampus. * $p < 0.05$, ** $p < 0.01$, *** $p < 0.001$, **** $p < 0.0001$ by one-way ANOVA with Holm-Sidak multiple comparisons testing.



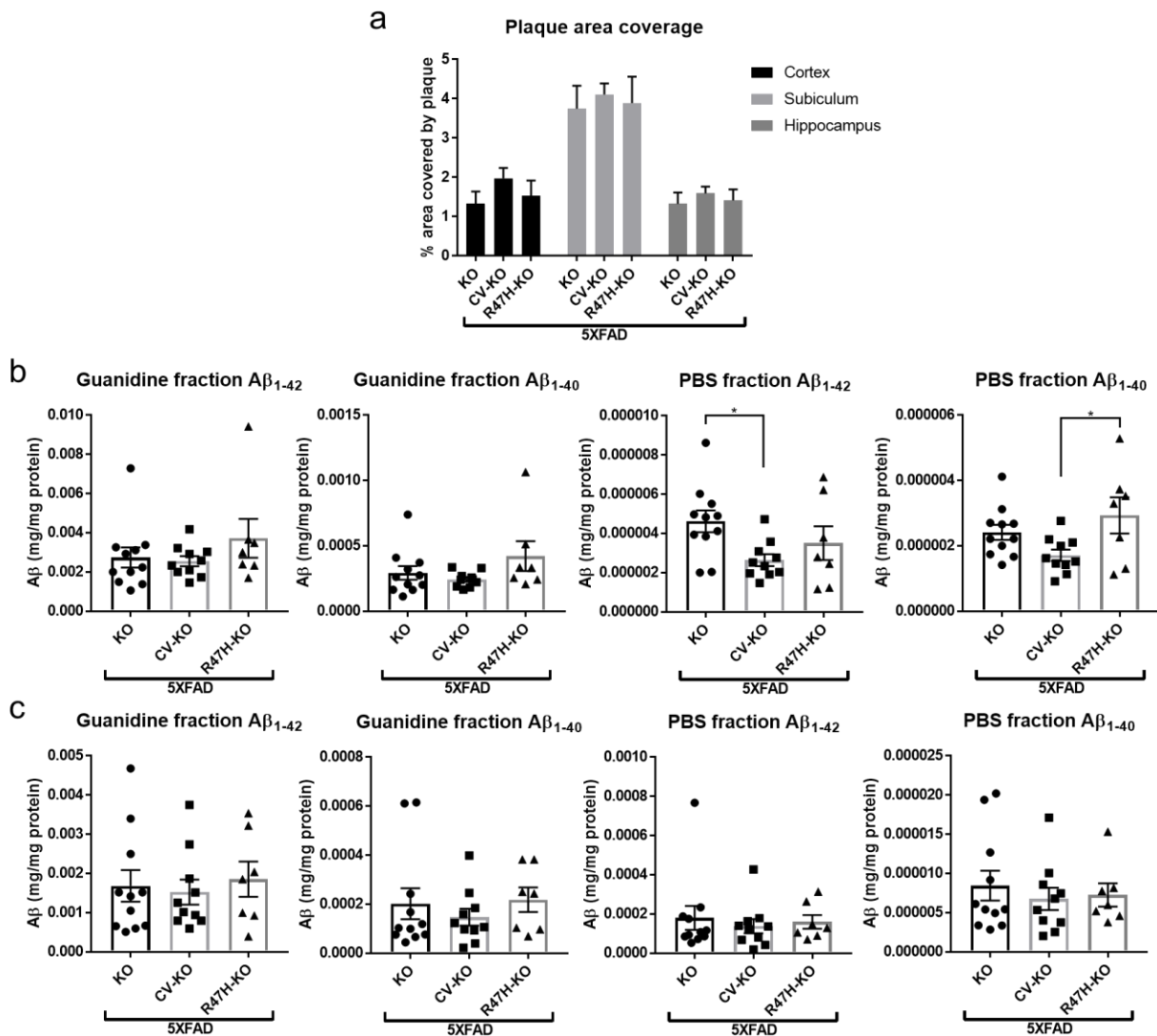


Figure 4. CV and R47H transgenes do not affect A β accumulation in the cortex or hippocampus. (A) Quantification of plaques by fluorescence microscopy of methoxy-X04 fibrillar plaques. (B,C) Quantification of A β 1-40 and A β 1-42 species in PBS-soluble and guanidine-soluble fractions of hippocampal (B) or cortical (C) homogenates.

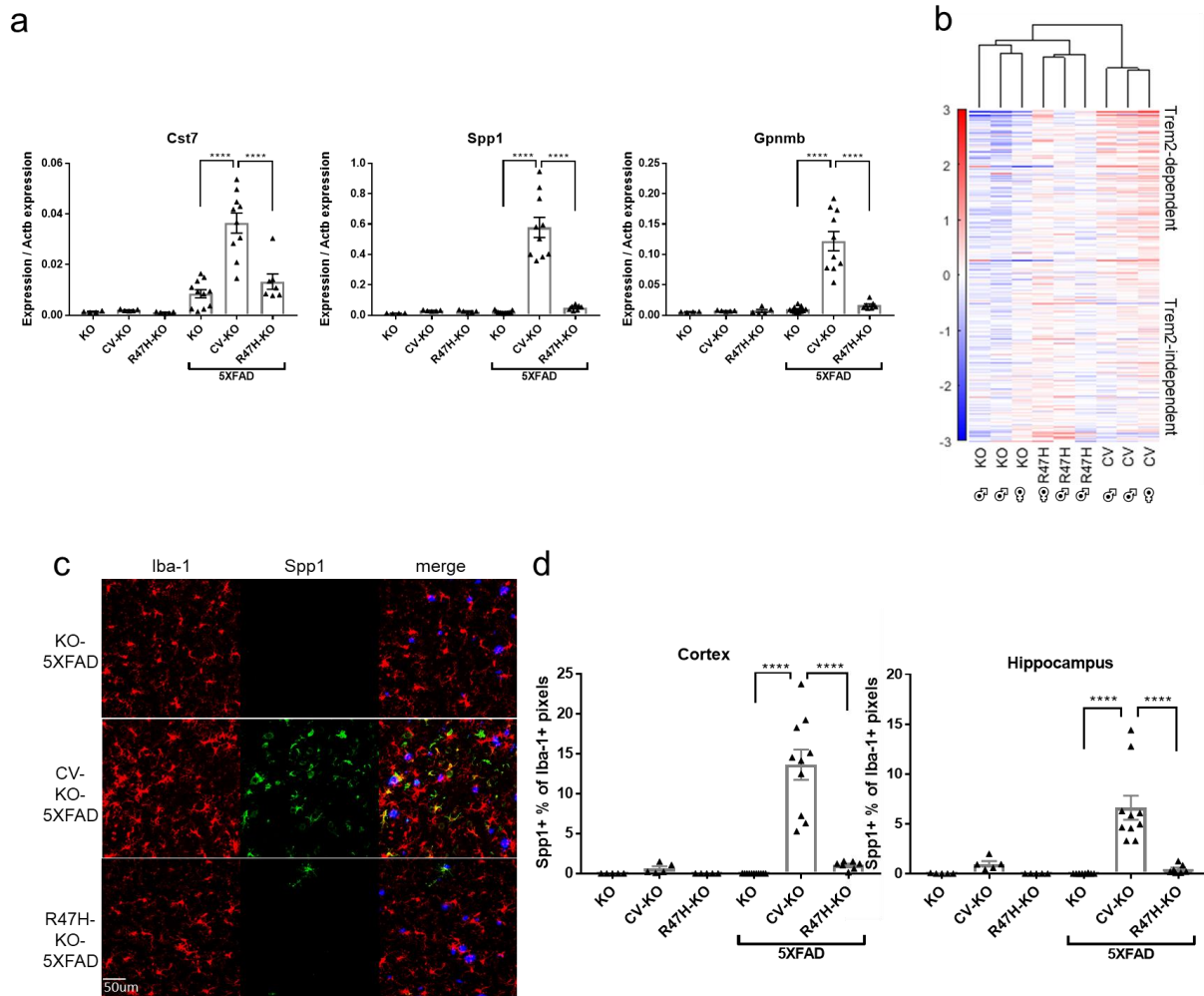


Figure 5. CV-KO-5XFAD mice have increased microglia activation compared to R47H-KO-5XFAD and KO-5XFAD mice.

(A) Quantitative RT-PCR on whole cortical tissue for neurodegeneration-associated microglial activation markers *Cst7*, *Spp1*, and *Gpnmb*, as well as classical inflammatory cytokines *Tnf*, *Il6*, and *Il1b*, showing dramatically higher microglial activation markers but not inflammatory cytokine transcripts in CV-KO-5XFAD compared to other groups. **(B)** Microarray analysis of activation markers in sorted microglia shows that KO-5XFAD and R47H-KO-5XFAD cluster together and separately from CV-KO-5XFAD. **(C)** *Spp1* protein is detected by confocal microscopy in CV-KO-5XFAD brains and largely absent from R47H-KO-5XFAD, KO-5XFAD, and non-5XFAD brains. **(D)** The percent of *Iba-1*⁺ (microglia) pixels that were also *Spp1*⁺ was quantified in cortex and hippocampus. * $p < 0.05$, ** $p < 0.01$, *** $p < 0.001$, **** $p < 0.0001$ by one-way ANOVA with Holm-Sidak multiple comparisons testing.

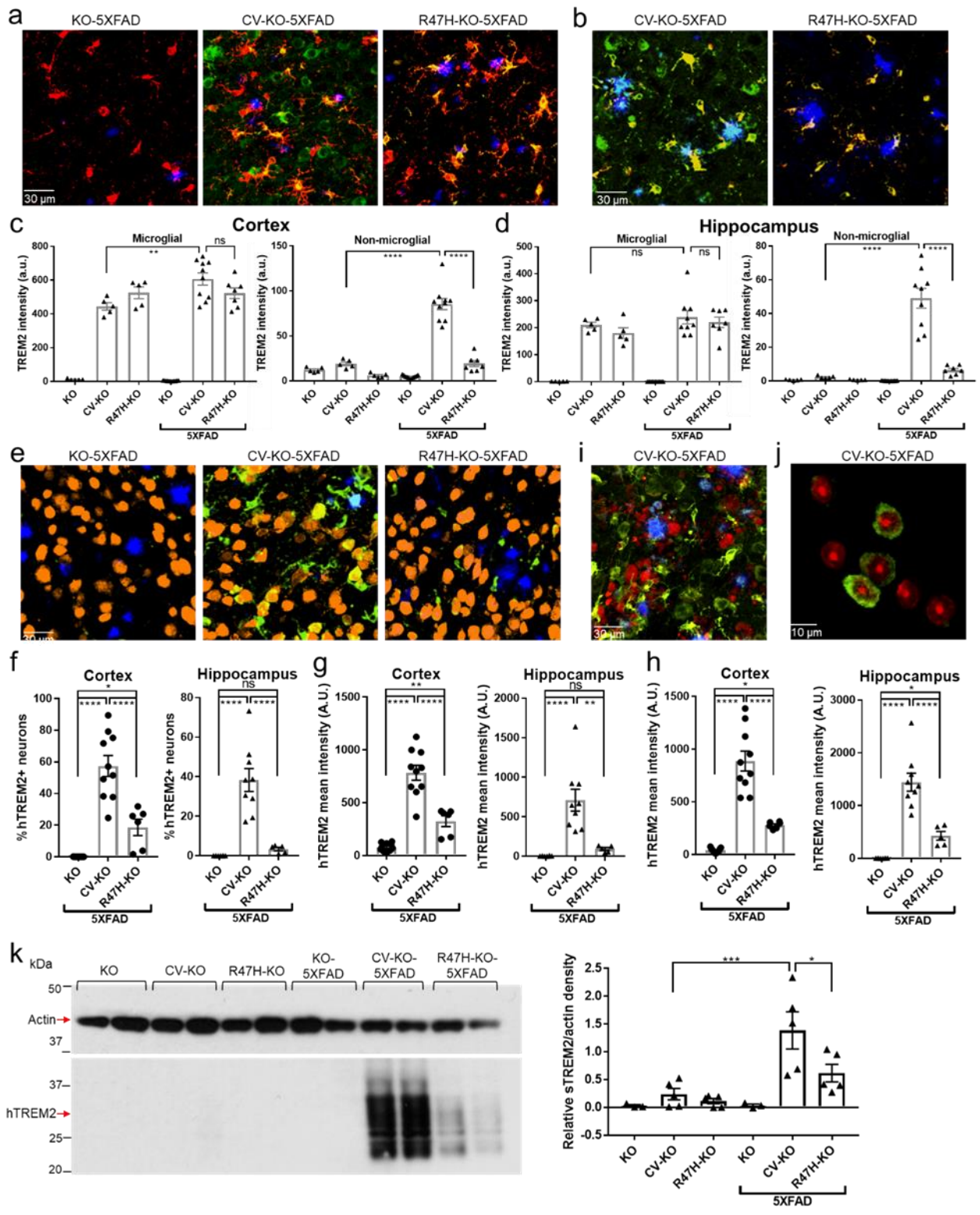


Figure 6. CV-KO-5XFAD shows unique localization of soluble hTREM2 to neurons, plaques, and other non-microglial spaces.

(A) Representative confocal images showing plaques (methoxy-X04, blue), microglia (Iba-1, red), and hTREM2 extracellular domain (ECD) (green) in the cortex. **(B)** Representative confocal images showing plaques (blue), hTREM2 C-terminus (red), and hTREM2 ECD (green). In CV-KO-5XFAD brains, hTREM2 ECD is present in voxels that lack either Iba-1 or hTREM2 C-terminus staining, whereas in R47H-KO-5XFAD, hTREM2 ECD largely colocalizes with Iba-1 and hTREM2 C-terminus. **(C, D)** Mean intensity of hTREM2 ECD staining was quantified in Iba-1-positive (microglial) voxels and Iba-1-negative (non-microglial) voxels in **(C)** cortex and **(D)** hippocampus, showing similar expression levels in microglia but a significant increase outside of microglia in CV-KO-5XFAD brains only. **(E)** Representative confocal images showing plaques (methoxy-X04, blue), neuronal soma (NeuN, orange), and hTREM2 (green). **(F)** Frequency of hTREM2+ neurons and **(G)** mean hTREM2 intensity in neuronal soma was quantified in cortex and hippocampus. **(H)** Mean intensity of hTREM2 staining was quantified in methoxy-X04+ plaques in cortex and hippocampus. hTREM2 ECD staining on plaques and neuronal soma was significantly higher in CV-KO-5XFAD compared to R47H-KO-5XFAD. **(I)** Representative confocal image of plaques (blue), APP+ dystrophic neurites (red), and hTREM2 ECD (green), showing a relative lack of soluble TREM2 on dystrophic neurites. **(J)** Representative confocal slice showing nuclei (ToPro-3, red) and hTREM2 ECD (green) within NeuN+ neuronal soma. hTREM2+ neurons do not show nuclear abnormalities characteristic of apoptosis. **(K)** Immunoblot of PBS-soluble fraction of hippocampal homogenates for hTREM2, showing a hTREM2 smear at lower molecular weight than full-length hTREM2, indicating soluble TREM2. Densitometric analysis normalized to actin was performed, showing that CV-KO-5XFAD mice had more soluble TREM2 than CV-KO and R47H-KO-5XFAD mice. * $p < 0.05$, ** $p < 0.01$, *** $p < 0.001$, **** $p < 0.0001$ by one-way ANOVA with Holm-Sidak multiple comparisons testing.

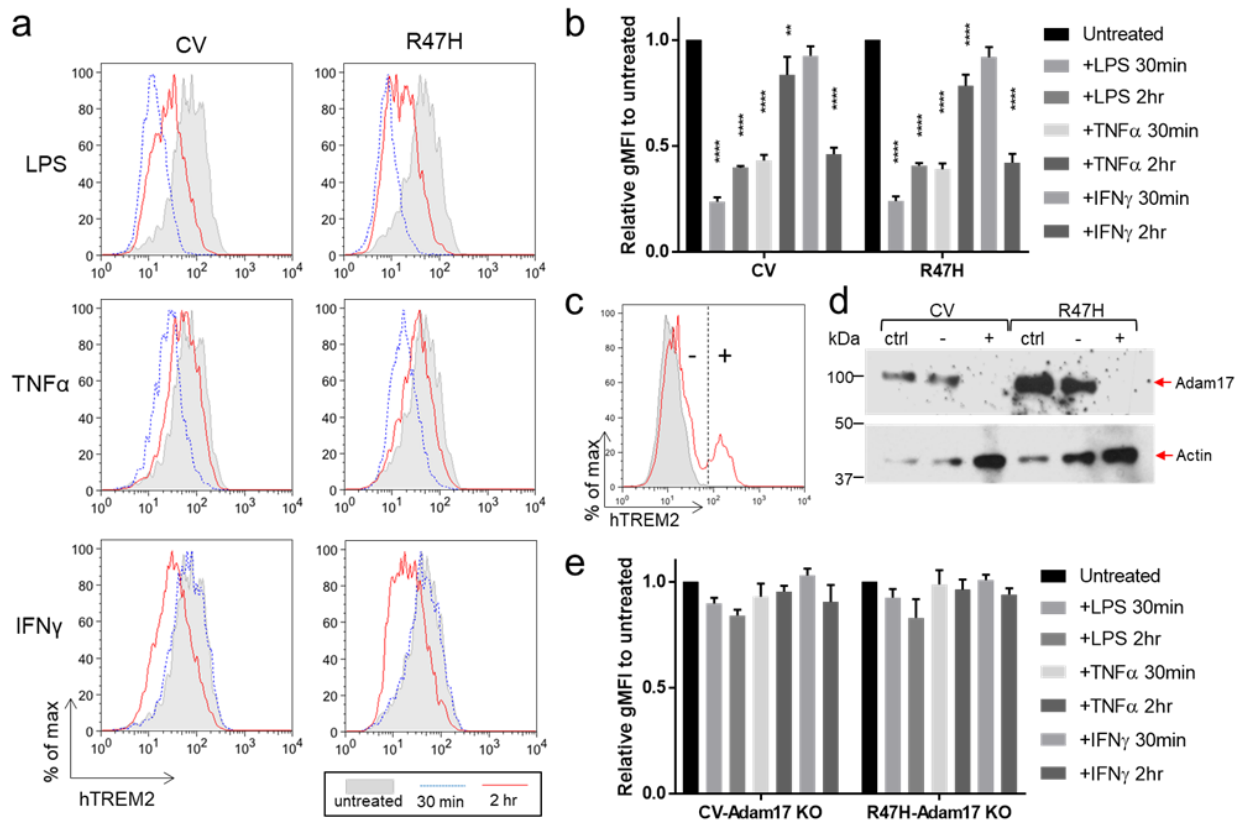


Figure 7. Various immunostimulatory signals induce similar CV and R47H hTREM2 cleavage from the cell surface.

(A) Representative flow cytometry plots demonstrating that both CV and R47H hTREM2 are lost from the cell surface of RAW264.7 upon treatment with LPS, TNF α , or IFN γ (untreated, gray shaded; 30 min., blue dashed line; 2 hr., red solid line). (B) Quantification of gMFI of LPS, TNF α , and IFN γ treated cells relative to untreated cells. Shown is mean \pm SEM for three independent experiments. (C) Adam17 was knocked out in CV- and R47H-expressing RAW264.7 cells. Non-transduced cells (ctrl; gray shaded) uniformly lost hTREM2 surface expression. Transduced cells (solid red line) had two populations, one that retained hTREM2 surface expression (+) and one that lost hTREM2 surface expression (-), and these two populations were sorted by FACS. (D) Immunoblot for Adam17. (E) Experiments conducted as in (a, b) using Adam17 KO. * $p < 0.05$, ** $p < 0.01$, *** $p < 0.001$, **** $p < 0.0001$ by one-way ANOVA with Holm-Sidak multiple comparisons testing.

Chapter 3: TREM2-dependent pathways in

activated microglia

A key outstanding question is how TREM2 facilitates microglial activation. While TREM2-deficient mice show defects in proliferation, survival, and plaque localization, the mechanistic basis for these defects is unknown. Understanding the mechanism of TREM2 function would shed light on potential therapeutic options targeting microglia in AD. Furthermore, the microglial response to neuropathology has often been viewed from the lens of M1 vs. M2 polarization, but the value of this paradigm for neurodegenerative disease has been challenged by recent studies of microglia acutely isolated from various models of neurodegeneration that suggest a common neurodegeneration-associated activation signature distinct from M1 or M2. As part of this activation signature, the most highly upregulated transcription factor is Bhlhe40, which is known to promote inflammatory responses in experimental autoimmune encephalitis. Most of this signature, including Bhlhe40, is ablated in TREM2-deficient animals in both the 5xFAD amyloid plaque model and the cuprizone-induced demyelination model. Thus, Bhlhe40 is a candidate on-switch that may contribute to microglial activation downstream of TREM2.

3.1 The role of TREM2 in microglia energy metabolism

To understand the mechanism by which TREM2 facilitates microglial activation in neurodegenerative states, we have expanded upon our recent findings that Dap12- or TREM2-deficient primary microglia and BMDMs show greater susceptibility to CSF-1 withdrawal. Previous studies had indicated that TREM2 can activate MAPK and calcium signaling; however, given the significant effect of growth factor signaling on the PI3K-Akt-mTOR pathway, we chose to quantify the effect of TREM2 deficiency on this pathway by Western blot. After culturing WT and TREM2-deficient BMDMs in standard or low CSF-1 conditions, we noted that CSF-1-deprived TREM2-deficient BMDMs showed a dramatic reduction in both mTORC1 and mTORC2 signaling, as measured by S6K phosphorylation, 4EBP phosphorylation, Akt S473 phosphorylation, and NDRG1 phosphorylation (**Fig. 8A**). Interestingly, CSF-1 deprived WT BMDMs showed a modest and variable reduction in these signaling events, suggesting to us that in this time frame, WT BMDMs could compensate for decreased CSF1R signaling through TREM2. To test this hypothesis, we cultured TREM2 reporter cells (as described in Aim 1.1) under normal culture conditions or with serum starvation to mimic CSF-1 deprivation. While reporter cells had a low level of activation under normal culture conditions, they robustly activated under starvation conditions, and this activation could be blocked by adding anti-TREM2 antibody (**Fig. 8B**). From these data, we conclude that TREM2 activity may increase during stressful conditions to compensate for decreases in mTOR signaling.

Given the essential role of mTOR in coordinating cellular metabolism and energy state, we decided to examine key cellular functions regulated by mTOR, namely autophagy and ATP production. We utilized the same experimental setup as before, using WT and TREM2-deficient

BMDMs cultured with standard or low CSF-1 overnight. Using the Seahorse analyzer, we measured baseline and glycolytic flux and oxidative phosphorylation at baseline and with stimuli that elicit maximum activity. Concordant with the exaggerated decrease in mTOR activity in CSF-1-deprived TREM2-deficient cells, baseline and maximal flux were relatively similar between WT and TREM2-deficient cells cultured in standard CSF-1 concentration, but TREM2-deficient cells progressively dropped below WT cells as CSF-1 concentration was lowered (**Fig. 8C**). ATP concentrations in cells cultured this way showed a similar pattern, with CSF-1-deprived TREM2-deficient having dramatically less ATP (**Fig. 8D**). Next, we measured autophagic flux in these cells by comparing the LC3-II/LC3-I ratio with or without the addition of bafilomycin, an inhibitor of lysosomal acidification. We found that indeed, LC3-II/LC3-I ratio was greatly increased specifically in CSF-1-deprived TREM2-deficient cells (**Fig. 8E**). Furthermore, when these cells were pelleted and examined by transmission electron microscopy, we noticed an accumulation of multilamellar vesicles consistent with autophagosomes (**Fig. 8F**). These findings show that TREM2-deficient cells are more susceptible to stress-induced low-energy state.

To elucidate the *in vivo* significance of these findings, we isolated microglia from WT and TREM2-deficient mice that were either on the 5XFAD mouse model or littermate controls. We performed Western blot and TEM analysis as described for BMDMs. Surprisingly, we found that microglia from non-5XFAD WT and TREM2-deficient mice, as well as from 5XFAD WT mice, had similar levels of phosphorylation of mTORC1 and mTORC2 target proteins, as well as similar LC3-II/LC3-I ratio, whereas 5XFAD TREM2-deficient microglia had dramatically reduced mTOR activity and increased LC3-II/LC3-I ratio (**Fig. 9A**). In addition, 5XFAD TREM2-deficient microglia had large numbers of multilamellar vesicles by TEM (**Fig. 9B**).

These results mirror our *in vitro* results with A β deposition substituting for CSF-1 deprivation, and strongly suggest that microglia exposed to amyloid pathology experience stress conditions that mimic CSF-1 deprivation in terms of mTOR suppression and induction of autophagy. Previously, it had been thought that TREM2-deficient microglia simply do not respond to A β pathology and resemble homeostatic microglia; however, our findings indicate that signaling pathways in A β -exposed TREM2-deficient microglia are dramatically altered compared to steady state. More generally, neurodegenerative disease appears to release cytotoxic signals that are normally counterbalanced by increased TREM2 signaling and reinforcement of the mTOR pathway.

To determine whether these *in vivo* defects are responsible for the reported phenotypes of TREM2-deficient mice in the 5XFAD model, we sought to restore mTOR signaling by stimulating pathways that bypass TREM2. We turned to our *in vitro* model of CSF-1-deprivation of BMDMs, in which we tried adding several candidate compounds into the culture during CSF-1 deprivation, using viability and metabolic measures as readouts of rescue. Many pattern recognition receptors initiate signaling cascades linked to mTOR. We found that addition of TLR agonists such as LPS, PAM3CSK4, and CpG could entirely rescue viability with CSF-1 deprivation in both WT and TREM2-deficient BMDMs (**Fig. 10A**). This was also true for TLR agonist-depleted zymosan, which activates Dectin-1 (**Fig. 10B**). Thus, alternative activating receptors could compensate for TREM2 *in vitro*. We also tested whether directly modulating metabolic parameters, even further downstream, could provide benefit in this system. Adding the creatine analog cyclocreatine led to a striking increase in viability in both WT and TREM2-deficient cells (**Fig. 10C**). Interestingly, while zymosan promoted ATP generation in cells,

cyclocreatine appeared rather to stabilize levels, significantly reducing ATP level in all groups except CSF-1-deprived TREM2-deficient cells, where it increased ATP level (**Fig. 10D**).

Because of previously reports utilizing cyclocreatine treatment in the brain, and the likely dramatic off-target effects of using TLR agonists *in vivo*, we administered cyclocreatine to WT and TREM2-deficient 5XFAD mice from the beginning of plaque formation at 2 months to the previously examined timepoint of 8 months as a microglial rescue experiment. Immunoblotting of sorted microglia from these groups showed that cyclocreatine-fed TREM2^{-/-}5XFAD mice had restored mTORC1 and mTORC2 activity and decreased autophagic flux by LC3II/LC3I ratio (**Fig. 11A**). In addition, microglia clustering around plaques was partially restored (**Fig. 11B**), as well as expression of the microglial activation marker Spp1 (**Fig. 11C**). Overall, these results demonstrate that TREM2 signaling impacts mTOR signaling and global microglia metabolism and downstream metabolic compensation can rescue the TREM2 phenotype. These findings provide a unifying mechanism for the diverse microglial functions affected by TREM2 deficiency. Importantly, cyclocreatine did not boost mTOR activity or Spp1 expression by itself but only in the TREM2^{-/-}5XFAD background, hinting that TREM2 downstream pathways are necessary but not sufficient to activate microglia.

3.2 Role of Bhlhe40 upregulation in microglial activation

We and others have previously defined a transcriptomic signature characteristic of microglial activation, part of which is dependent on TREM2. Among these genes, the most highly upregulated transcription factor, in multiple datasets, is Bhlhe40. In particular, Bhlhe40 is strongly upregulated in the 5XFAD model compared to other genes (**Table 2**). This gene has

been linked to pro-inflammatory responses in other immune cells¹⁶⁰ and is not expressed in steady-state microglia, suggesting that it could be an on-switch that controls part of the activation signature.

First, we attempted to directly visualize the pattern of *Bhlhe40* expression by crossing *Bhlhe40*-EGFP mice to 5XFAD mice. Unfortunately, we found by confocal microscopy that while other cells such as some neurons and astrocytes express EGFP at detectable levels at steady state and in the 5XFAD model, microglia do not, even surrounding plaques (**Fig. 12**). These results suggest that while *Bhlhe40* may be upregulated during disease, the final expression level is still far less than other cells that express *Bhlhe40*. Even so, *Bhlhe40* could be controlling some microglial activation genes. Therefore, we bred *Bhlhe40*-deficient mice to 5XFAD mice and analyzed mice with abundant pathology, around 9 months old.

The most direct measure of *Bhlhe40* function, given that *Bhlhe40* is a transcription factor, would be to analyze transcriptional changes in microglia during disease. Therefore, we sorted microglia from *Bhlhe40*^{+/+} and *Bhlhe40*^{-/-} 5XFAD brains and performed microarray analysis. In accordance with the low expression seen in *Bhlhe40*-EGFP microglia, few significant differences were detected between the two genotypes (**Fig. 13A**), and genes that were altered did not have any obvious relationship or large fold changes. Examination of microglial genes known to be altered in the 5XFAD model showed that activation genes such *Spp1*, *Gpnmb*, and *Cst7* were indeed expressed in all samples, but equally between genotypes (**Fig. 13B**). Interestingly, microglia clustering around plaques was more pronounced in the *Bhlhe40*^{-/-} mice. (**Fig. 14A**). Furthermore, astrocyte clustering around plaques, which is affected by microglial clustering, was also increased, but not significantly (**Fig. 14B**). Thus, we conclude that *Bhlhe40* is not expressed highly in microglia and is dispensable for the microglia response to

A β plaques, but it may serve to dampen inflammatory responses through effects in other cell types. Based on lists of genes upregulated in activated microglia, there do not seem to be other transcription factors that “switch on” during disease, suggesting that perhaps the transcriptional program of activated microglia is mediated instead by post-translational effects or downregulation of transcription factors.

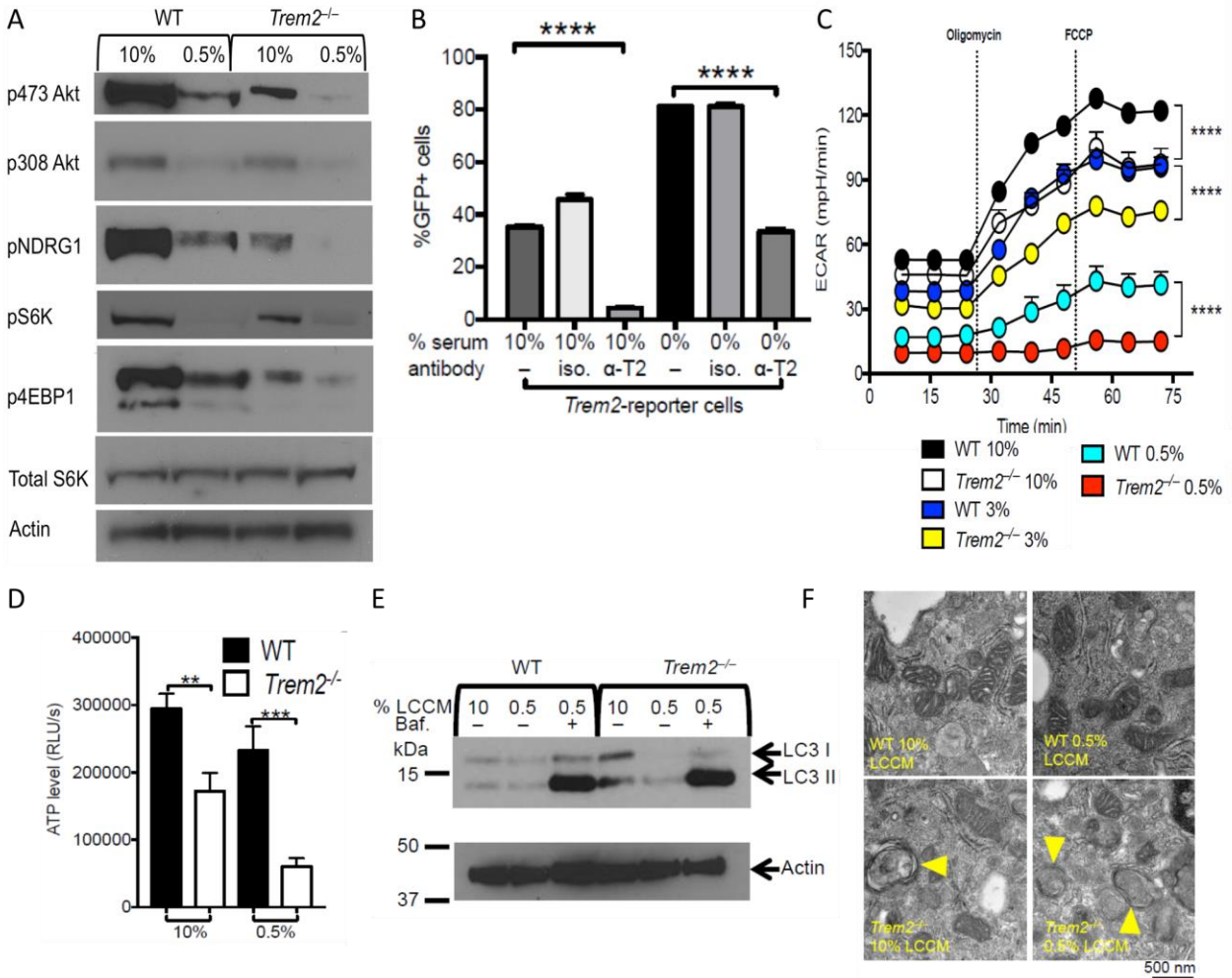


Figure 8. TREM2-deficient BMDMs show increased sensitivity of mTOR-dependent cell functions to growth factor deprivation.

(A) CSF-1 deprived (0.5% L-cell conditioned medium) TREM2-deficient BMDMs have significantly lower mTORC1 and mTORC2 activity as measured by Akt, NDRG1, S6K, and 4EBP1 phosphorylation. (B) Serum-starved TREM2 reporter cells increase activation of TREM2 relative to 10% serum conditions. (C) ECAR is lower in TREM2-deficient BMDMs compared to WT BMDMs and becomes progressively lower with decreasing CSF-1 concentration. (D) ATP levels are dramatically decreased in CSF-1 deprived TREM2-deficient BMDMs. (E) LC3-II/LC3-I increases dramatically in CSF-1 deprived TREM2-deficient BMDMs and reflects increased autophagic flux as shown by addition of bafilomycin. (F) TEM images of BMDMs reveals presence of multilamellar vesicles in TREM2-deficient BMDMs, characteristic of autophagosomes. * $p < 0.05$, ** $p < 0.01$, *** $p < 0.001$, **** $p < 0.0001$ by one-way ANOVA with Holm-Sidak multiple comparisons testing.

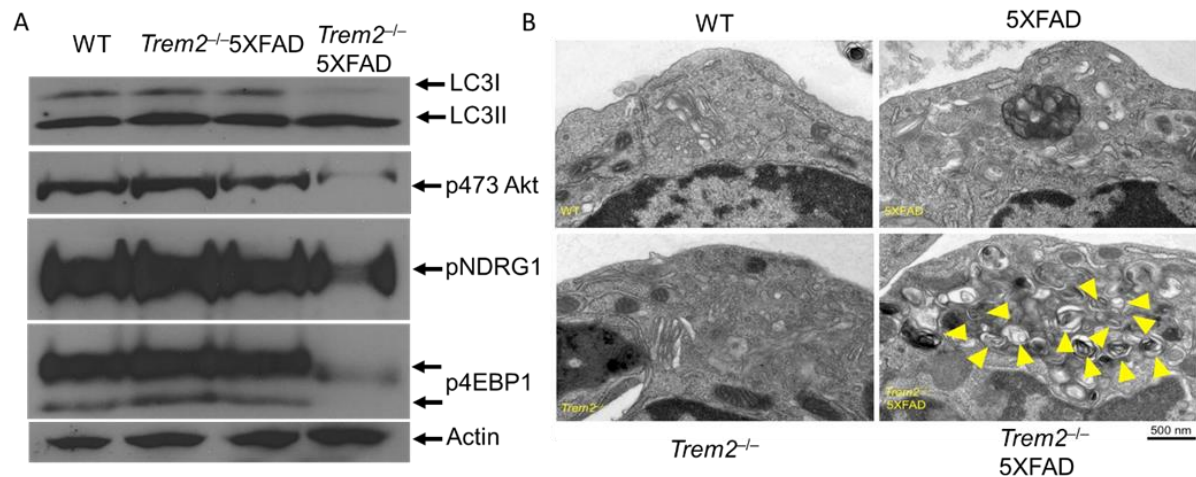


Figure 9. TREM2-deficient microglia exhibit suppressed mTOR activity and increased autophagy in vivo in the 5xFAD model.

(A) Western blot of sorted microglia from WT or TREM2-deficient mice with or without the 5xFAD transgene shows similar phosphorylation of mTOR effector genes in all groups except TREM2-deficient 5xFAD, which has much lower activity. On the other hand, LC3-II/LC3-I ratio is greatly increased in this group. (B) TEM of pelleted sorted microglia from these groups.

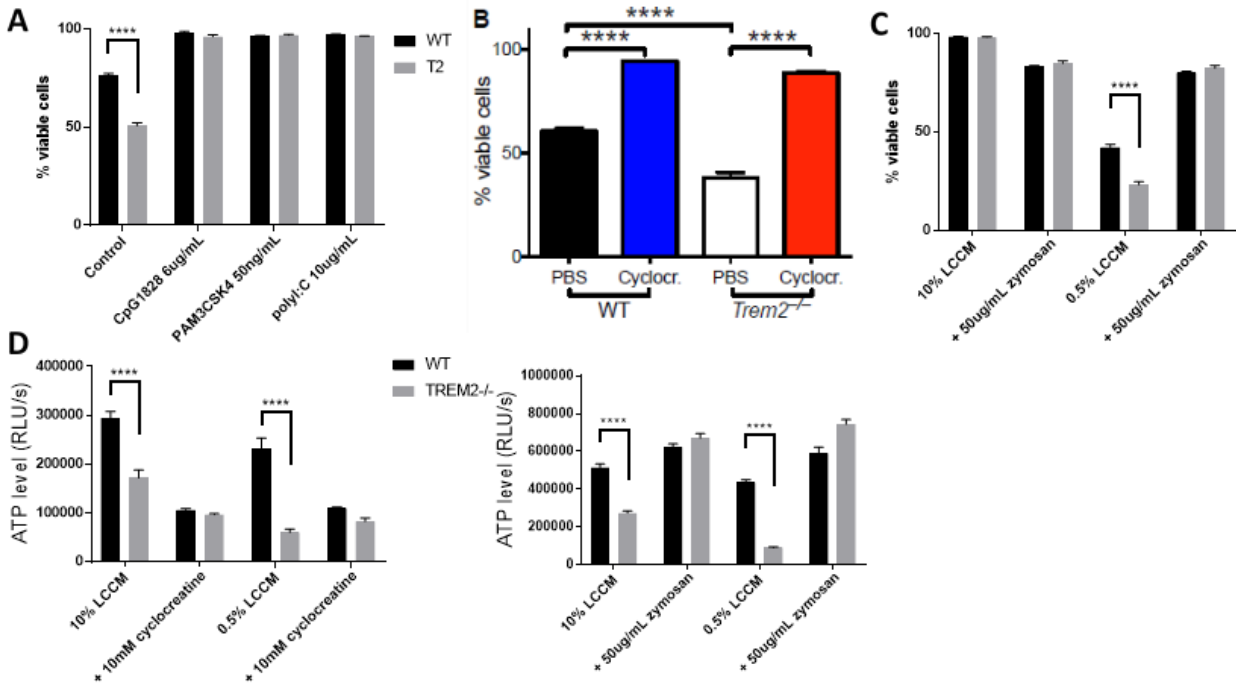


Figure 10. Alternative pathways can compensate for sensitivity to CSF-1 deprivation associated with TREM2 deficiency.

(A) TLR agonists, (B) cyclocreatine, and (C) depleted zymosan can fully restore viability in CSF-1 deprived WT and TREM2-deficient BMDMs. (D) Cyclocreatine normalizes ATP concentration for all conditions, while zymosan greatly boosts ATP concentration in all conditions. * $p < 0.05$, ** $p < 0.01$, *** $p < 0.001$, **** $p < 0.0001$ by one-way ANOVA with Holm-Sidak multiple comparisons testing.

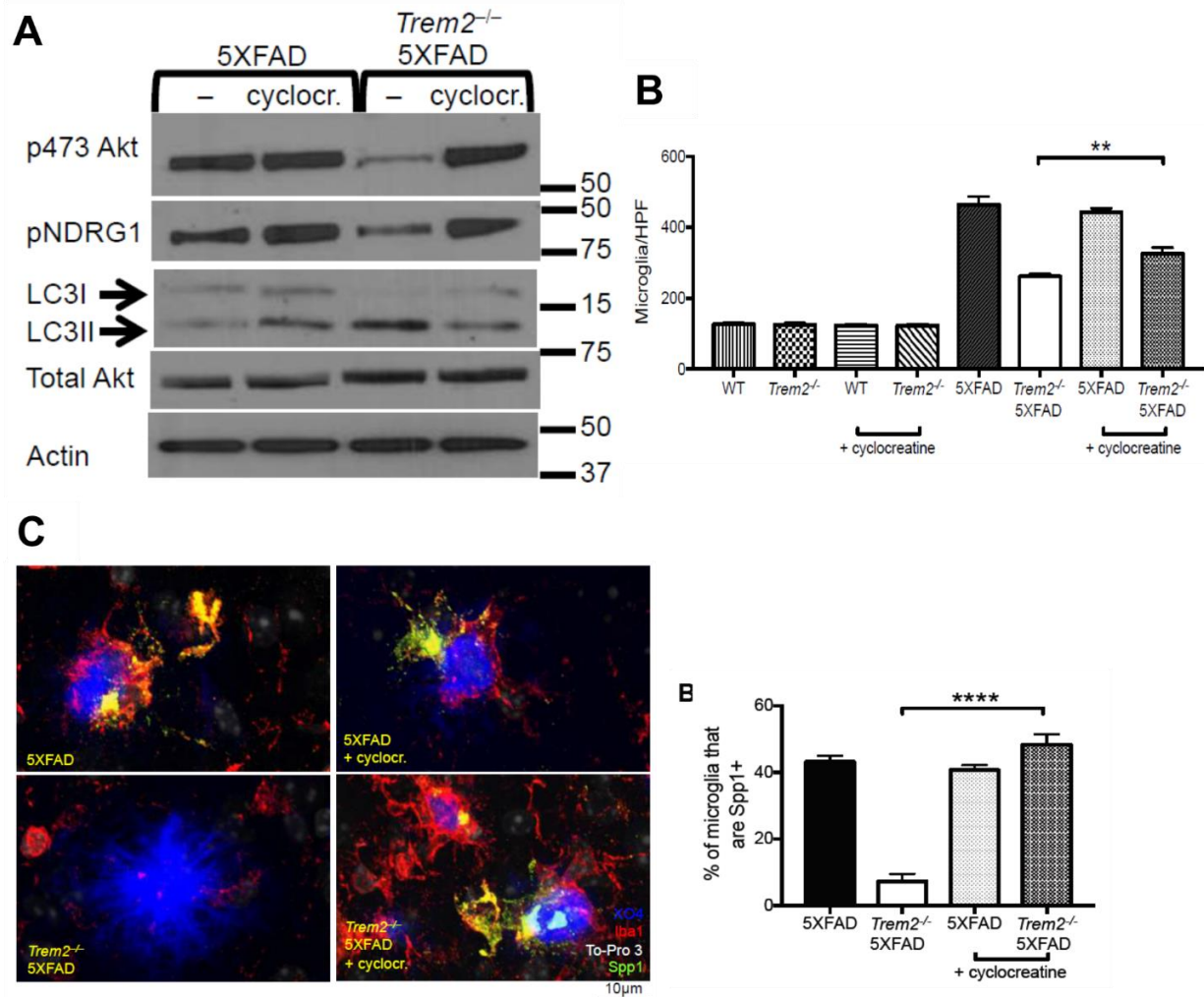


Figure 11. Cyclocreatine treatment partially restores microglia function in TREM2-deficient 5XFAD mice.

(A) Immunoblotting for mTOR targets Akt S473 and NDRG1, as well as LC3-I and LC3-II in non-treated and cyclocreatine-treated 5XFAD. (B) Microglia number in TREM2-deficient 5XFAD is partially restored to 5XFAD levels with cyclocreatine treatment. (C) The percentage of microglia expressing activation marker Spp1 is rescued by cyclocreatine treatment. * $p < 0.05$, ** $p < 0.01$, *** $p < 0.001$, **** $p < 0.0001$ by one-way ANOVA with Holm-Sidak multiple comparisons testing.

Table 2. Genes upregulated in 8 month 5xFAD microglia compared to controls.

	WT 5xFAD/ctrl	TREM2 5xFAD/ctrl
Gpmb	51.1348009	5.844581907
Spp1	32.80583834	2.161398446
Fabp3	29.91093348	3.927947952
Mamdc2	28.38995648	1.401424397
Cst7	27.18838572	14.19932165
Fabp5	26.92798746	4.081234505
Hpse	22.57314185	5.228671278
Lpl	22.56346182	4.988805449
Egln3	22.37373468	2.73306839
Bhlhe40	19.62798126	1.67423832
Igf1	18.77155118	4.381045471
Itgax	17.85544881	3.226909598
Atp6v0d2	14.944863	1.166452117
Actr3b	12.5927362	2.205279913
Ch25h	12.15845162	2.044315642
Tnfsf9	12.01862098	2.574841367
Clec7a	11.66986089	4.614432883
Etl4	11.3741753	1.903113427
Axl	10.93860924	2.525070146
Cd200r4	10.9067322	3.005780224
Cox6a2	10.36107115	3.434451054
Cd69	10.20685209	3.07515763

Fold change was calculated for both WT and TREM2-deficient mice, and genes are sorted by greatest fold change. Bhlhe40 is highlighted in red.

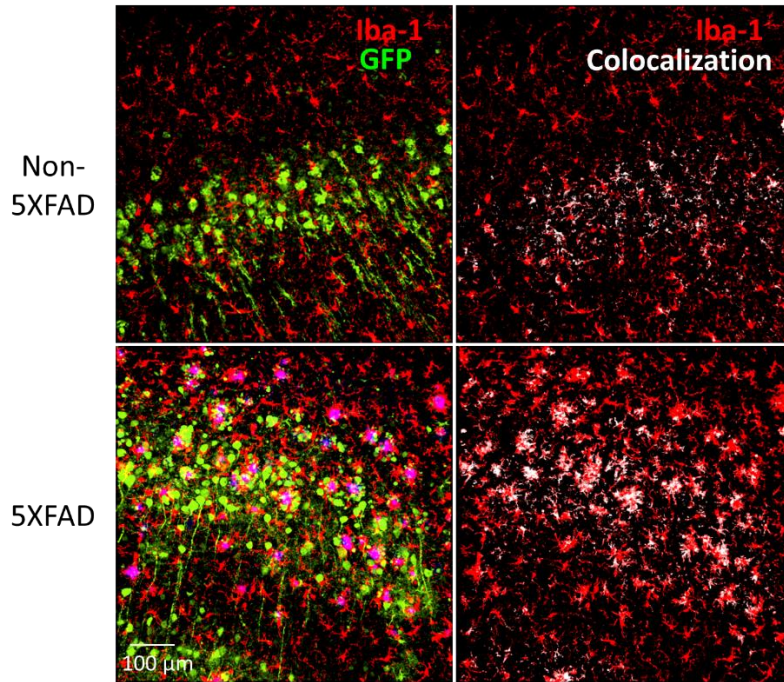


Figure 12. Bhlhe40-EGFP reporter mice have little Bhlhe40 expression in microglia. The left side shows GFP and Iba-1 co-staining, and the right side shows only the GFP signal colocalized to microglia. While some colocalization of GFP and Iba-1 is present, it is likely artifactual as it corresponds to regions of GFP⁺ neurons.

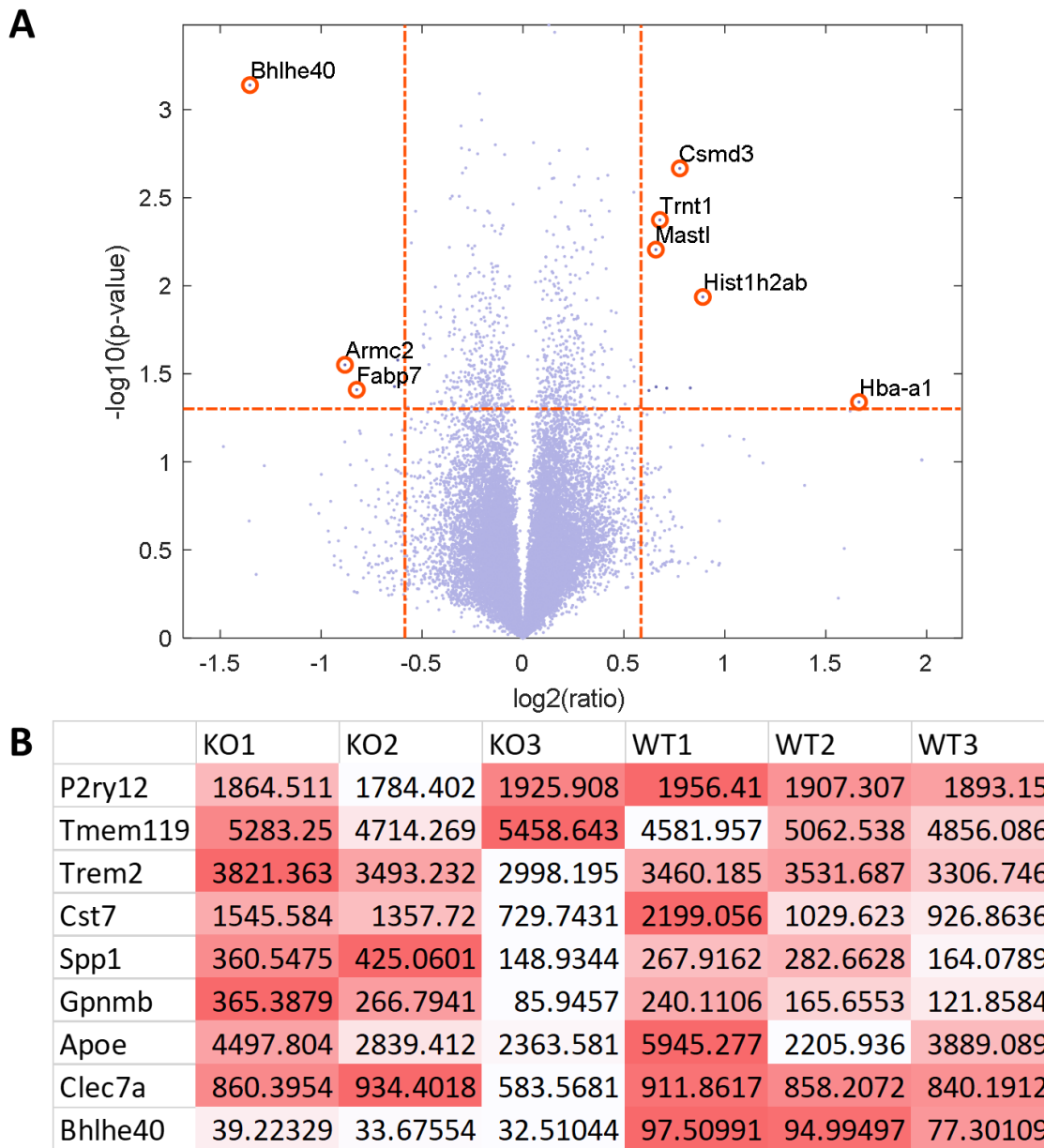


Figure 13. Bhlhe40 deficiency does not affect activation state of sorted microglia on the transcriptional level.

(A) Volcano plot showing Bhlhe40^{-/-}/WT fold change and p-value, with thresholds of differential expression set at 1.5 fold-change and p<0.05. Only a handful of genes are differentially expressed with these criteria, including Bhlhe40. (B) Quantile-normalized values of a panel of genes altered during microglial activation, color-coded within each row (red is higher expression). Homeostatic and activated microglia genes are expressed in both genotypes at similar levels.

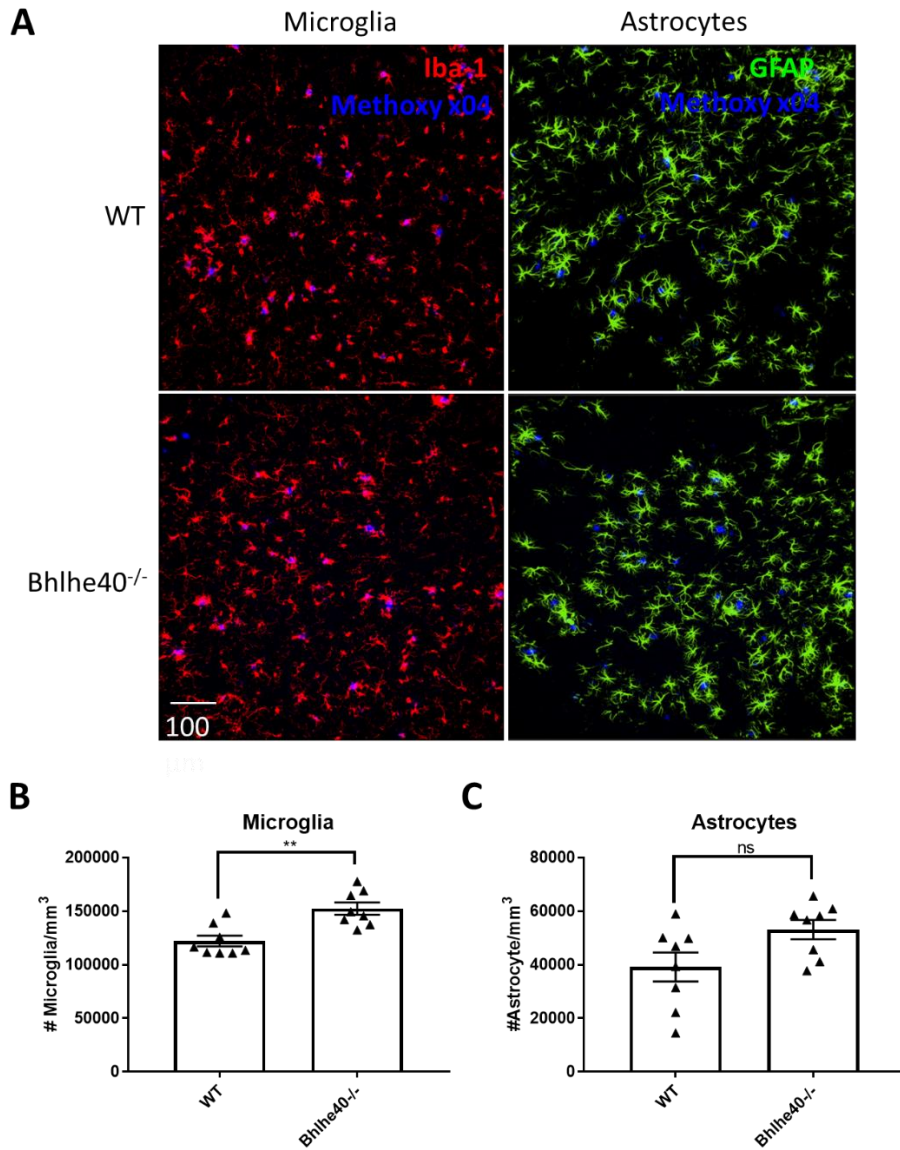


Figure 14. Microglia and astrocyte clustering around plaques is altered by Bhlhe40 deficiency. (A) Representative images of microglia, astrocytes, and A β plaques in 5XFAD and Bhlhe40^{-/-} 5XFAD mice, showing microglia and astrocytes surrounding plaques in both genotypes. (B) The density of microglia within 20 μ m of plaques is higher in Bhlhe40^{-/-} mice. (C) A similar trend is observed with astrocytes but is more variable.

Chapter 4: Unbiased screen for TREM2

expression-modifying genes

Given that dose-dependent effects of TREM2 deficiency have been observed in mouse models of AD^{40,161,162} and that heterozygosity for TREM2 mutations can increase AD risk, disease progression appears to be quite sensitive to changes in TREM2 expression. Thus, modulation of TREM2 expression levels may offer an alternative strategy for harnessing protective functions of TREM2. Increasing TREM2 expression has the advantage of preserving the spatiotemporal activation profile of TREM2. For instance, if TREM2 specifically recognizes amyloid plaque components, then increased TREM2 expression would sensitize plaque-adjacent microglia to activation while limiting unnecessary inflammation elsewhere. Early work on TREM2 reported that IL-4 can increase TREM2 surface expression, while LPS or IFN γ can cause complete loss of expression⁵⁶. As previously mentioned, the extracellular domain of TREM2 can be shed by ADAM10 and ADAM17 during steady state, reducing the surface TREM2 available for intracellular signaling. However, beyond these relatively isolated mechanisms, little is known about regulation of TREM2 surface expression.

4.1 Design and execution of CRISPR-Cas9 knockout screen

CRISPR-Cas9 knockout library screening has emerged as a powerful, versatile tool for identifying causal genes and pathways important for various processes. By performing a gene

knockout screen for TREM2 surface expression, we can obtain a global snapshot of pathways that regulate TREM2 synthesis, trafficking, and degradation, which has not previously been attempted. These results would allow us and others to pursue better-targeted therapeutics to boost TREM2 expression. Furthermore, some of these pathways likely regulate other proteins in different cell types, and mechanistic understanding of the effect of these genes or pathways on TREM2 will help to elucidate their effect in general in other systems.

To identify genes that modulate TREM2 surface expression, we used the microglia-derived BV2 cell line, which expresses abundant surface TREM2. We took advantage of a previously generated set of four independent BV2 CRISPR-Cas9 lentiviral knockout libraries, each containing one single-guide RNA (sgRNA) per gene targeting a total of 20,077 genes. These libraries are each subpools of the published Asiago library¹⁶³. Each clone in this library contains Cas9, a unique sgRNA, and the corresponding gene ablation. Clones can be isolated according to phenotypic enrichment, then assayed for genotypic enrichment by amplification and sequencing of the lentivirally integrated sgRNA. Since surface expression is a cell-intrinsic phenotype that can be assessed by flow cytometry, we performed a pooled screen whereby cells staining for relatively higher or lower levels of TREM2 were sorted from the starting library by FACS to identify enriched sgRNAs. After sorting the 20% highest and 20% lowest TREM2-expressing cells, we cultured TREM2-high and TREM2-low cells to equilibrate them and sorted either the 20% highest or 20% lowest. This process was repeated one additional time, for a total of three sequential sorts. A portion of cells from each step was harvested for genomic DNA, and all samples were submitted for amplification and sequencing at the Genomic Perturbation Platform at the Broad Institute. The master list of hits was assembled in three steps. First, we calculated fold enrichment of each gene within each subpool as follows: read count values were

averaged for singly, doubly, and triply sorted TREM2-high or TREM2-low samples, and the ratio of TREM2-high : TREM2-low was calculated. This method favors sgRNAs that enrich strongly after multiple sorts but also those that are consistently enriched after each step. Second, we calculated a modified rank mean for each gene across the four subpools by dropping the worst rank and averaging the other three. Third, we determined statistical significance by simulating random rank lists and empirically calculating the chance that a randomly generated rank list would produce a modified rank mean as good or better than the given modified rank mean. A cut-off of $p < 0.05$ was used to select genes for follow-up.

As expected, TREM2 and DAP12 sgRNAs were among the top three most enriched in TREM2-low populations, while ADAM17 sgRNAs were the most enriched in TREM2-high populations. Thus, our screen easily detected known modulators of TREM2 surface expression, and an additional 25 genes had statistically significant rank sums (**Table 3**). These genes were validated by lentiviral expression of individual sgRNAs and staining for surface TREM2. The top-scoring sgRNA for each gene was selected from the four pools and inserted into the lentiGuide-puro construct, and lentivirus was packaged and transduced into Cas9-expressing BV2 cells. Due to generation of a heterozygous cell population by CRISPR knockout, each transduced population, including vehicle-transduced controls, were sorted once for either the highest or lowest 20% of TREM2 expressers, depending on the direction of change predicted by the screen, to enrich for clones with the largest effects (presumably homozygous knockouts). For example, the TREM2 and DAP12 knockout lines were sorted for low expressers, and the ADAM17 knockout line was sorted for high expressers. These once-sorted lines were then used to quantify mean fluorescence intensity (MFI) relative to once-sorted empty vector cells. Several sgRNAs caused statistically significant differences in MFI in the expected direction (TREM2,

DAP12, DOK1, SLC35A3, NMT1, CRKL, TMEM131), but effect sizes were generally small for novel genes (**Fig. 15**). Further validation of these genes with a second, independent sgRNA confirmed only DAP12, ADAM17, and TMEM131 (**Fig. 16A**).

4.2 *In vitro* characterization of TMEM131 effect on TREM2

We decided, for practical purposes, to focus specifically on the most promising hit, TMEM131. First, to confirm the specificity of TMEM131 knockout, we used another independent sgRNA against TMEM131 and demonstrated again increased TREM2 surface expression. We cloned out TMEM131 cDNA from murine brain tissue and overexpressed a 3xFLAG-tagged version in BV2; TREM2 surface expression decreased, confirming the specificity of TMEM131 (**Fig. 16B**). We sought to interrogate the dependence of the TMEM131-TREM2 interaction on transcriptional regulation, on species, and on cleavage. First, we treated various CRISPR-Cas9 knockout lines with the broad metalloproteinase inhibitor GM6001. If TMEM131 functions by modulating ADAM family metalloproteinases, then in the presence of GM6001, the difference between TMEM131 knockout and parental BV2 should be reduced. This treatment increased the TREM2 surface expression in all cell lines, including TMEM131 knockout to a similar extent, making this mechanism less likely (**Fig. 16C**). Next, we replaced the stem region of human TREM2 with the stem region of human CD8, which is not cleaved by ADAM family members. This construct was overexpressed in BV2 cells under control of the CMV promoter and demonstrated relatively homogeneous and abundant surface expression. After lentiviral transduction with two independent sgRNAs targeting TMEM131 or empty

vector, TMEM131 knockout cell lines expressed significantly higher levels of CMV-driven, cleavage-resistant human TREM2 (**Fig. 16D**), demonstrating that TMEM131 cross-reacts with both human and mouse TREM2 and likely does not function through transcriptional regulation or cleavage of the stem region. Because of the robust expression of the cleavage-resistant construct and the availability of reagents against human TREM2, we used these cell lines for subsequent experiments.

Given these results, we hypothesized that TMEM131 likely regulates TREM2 in a post-translational fashion. First, we investigated if TMEM131 affects the half-life of surface TREM2 by performing a cycloheximide chase. While TMEM131 knockout cells express higher surface TREM2 at baseline, they lose expression at a similar rate over the course of a two hour chase, suggesting that TMEM131 does not directly promote degradation of mature surface TREM2 (**Fig. 17A**).

Because of the unique presence of intramembranous charged residues in TREM2 and Dap12 that are important for TREM2 trafficking, we investigated whether this feature was important for TMEM131-TREM2 interaction by generating a TREM2 mutant with a K→A substitution that ablates the intramembranous charge. This mutation is also expected to abolish interaction of TREM2 with DAP12. We found that TREM2 K186A surface expression increased upon TMEM131 knockout similarly to non-mutated TREM2 (**Fig. 17B**). This demonstrates that the K186 residue is not required for TMEM131 effect, and most likely, TMEM131 interacts directly with TREM2 rather than indirectly through Dap12. We performed additional experiments testing the specificity of TMEM131 effect by measuring surface expression of other myeloid markers such as CD11b, CD33, CD44, and CD45 with or without TMEM131 knockout. None of these surface markers were affected, showing that the effect on TREM2 is relatively

specific (**Fig. 17C**). These results provide a rough idea of the role of TMEM131 in regulating TREM2 surface expression and set the stage for future *in vivo* studies.

Table 3. List of genes and modified rank mean for statistically significant genes enriched in TREM2-low or TREM2-high fractions.

sgRNA enriched in TREM2-low						sgRNA enriched in TREM2-high	
Gene	Rank mean	Gene	Rank mean	Gene	Rank mean	Gene	Rank mean
Trem2	1	Pten	10.33	1110025L11Rik	54	Adam17	22
Dok1	2	Ptpn6	16	Krtap6-5	57.33	Tecr	22.33
Tyrobp	2.67	Pitpnb	18.67	Nadk	74.67	Gne	57.67
Ric8	5.33	Son	20	Nmt1	76.33	Tmem131	66.67
Kctd5	6.33	Ggnbp2	30	Krtap19-2	81.67	Slc35a1	98
Slc35a3	6.67	Dnttip1	32.5	Tec	84.33		
Crkl	7.67	Inpp5d	41.67	Fasn	94		
Tfap4	8.33	Ppp2r4	44.33				

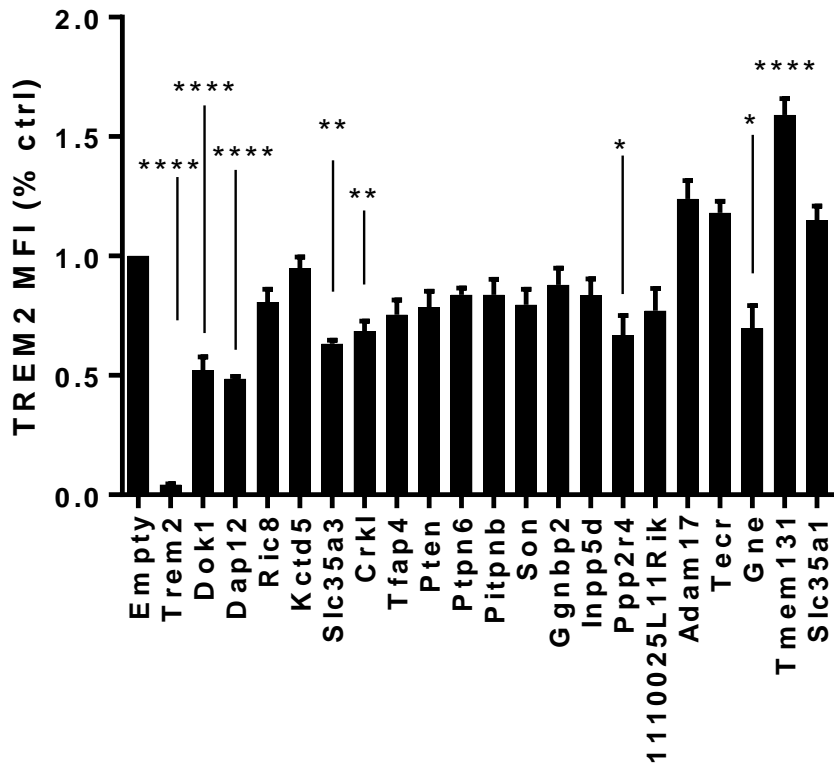


Figure 15. Statistically significant genes were validated by generating sgRNA knockouts using the top-ranking sgRNA from the screen.

As expected, TREM2 sgRNA effectively ablates TREM2 surface expression, while DAP12 and ADAM17 knockout decreases and increases TREM2 surface expression, as expected. Of novel genes, DOK1 knockout has the largest effect in reducing TREM2 surface expression, while TMEM131 knockout has the largest effect in increasing it. * $p < 0.05$, ** $p < 0.01$, *** $p < 0.001$, **** $p < 0.0001$ by one-way ANOVA with Holm-Sidak multiple comparisons testing.

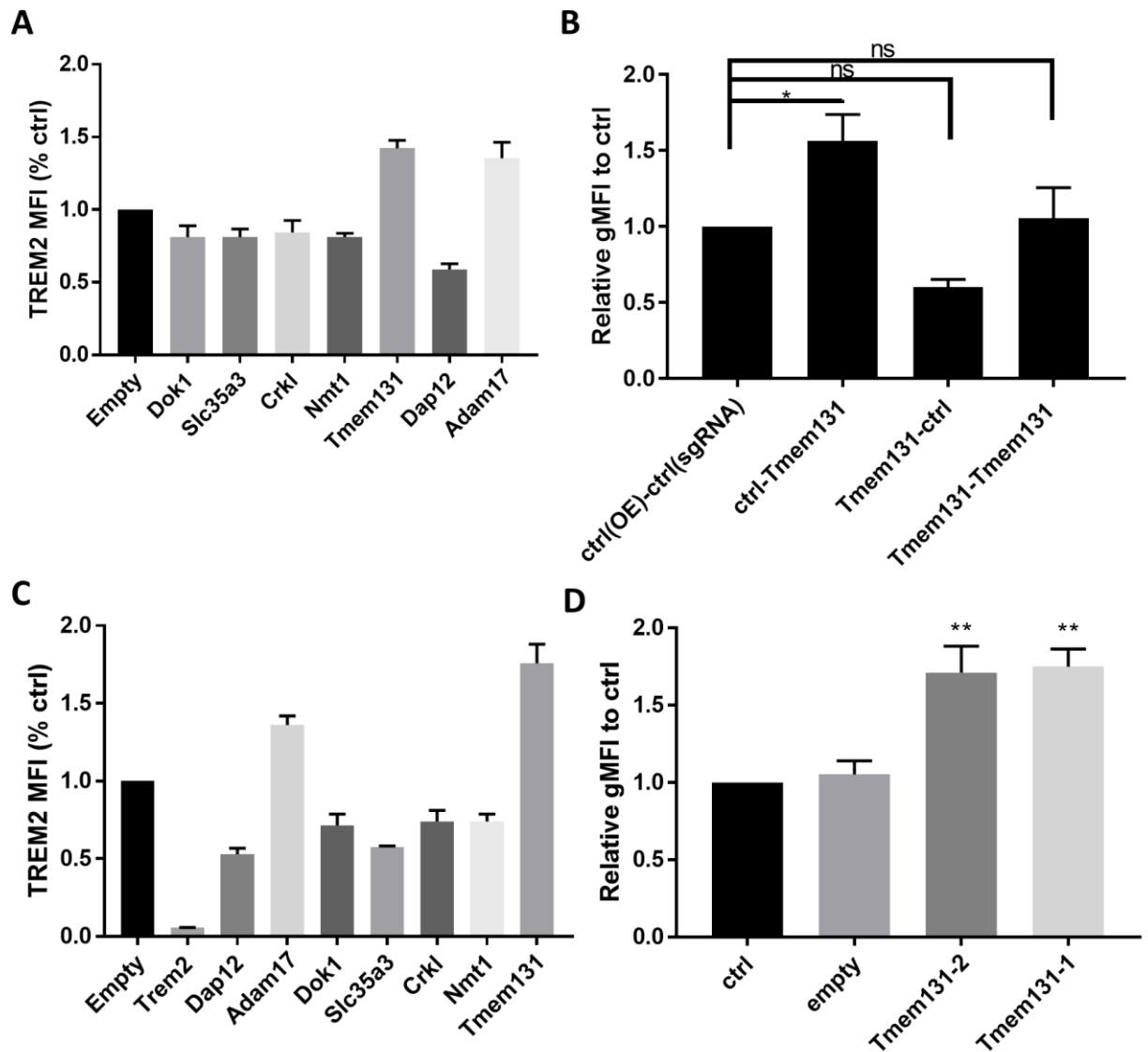


Figure 16. TMEM131 suppresses surface levels of TREM2 through a metalloproteinase-independent mechanism.

(A) Lentiviral CRISPR-Cas9 knockout of genes passing first-round validation with a second, independent sgRNA further validates TMEM131 suppression of surface TREM2 level. (B) Retroviral overexpression of TMEM131-3XFLAG in TMEM131-KO BV2 cells restores normal TREM2 levels and reduces TREM2 levels further in WT BV2 cells. (C) Treatment of CRISPR KO BV2 lines with broad metalloproteinase inhibitor GM6001 boosts surface TREM2 levels across cell lines but preserves the higher relative expression in TMEM131-KO cells. (D) Cleavage-resistant human TREM2 expressed under CMV promoter in BV2 cells can be increased by TMEM131-KO with two independent sgRNAs.

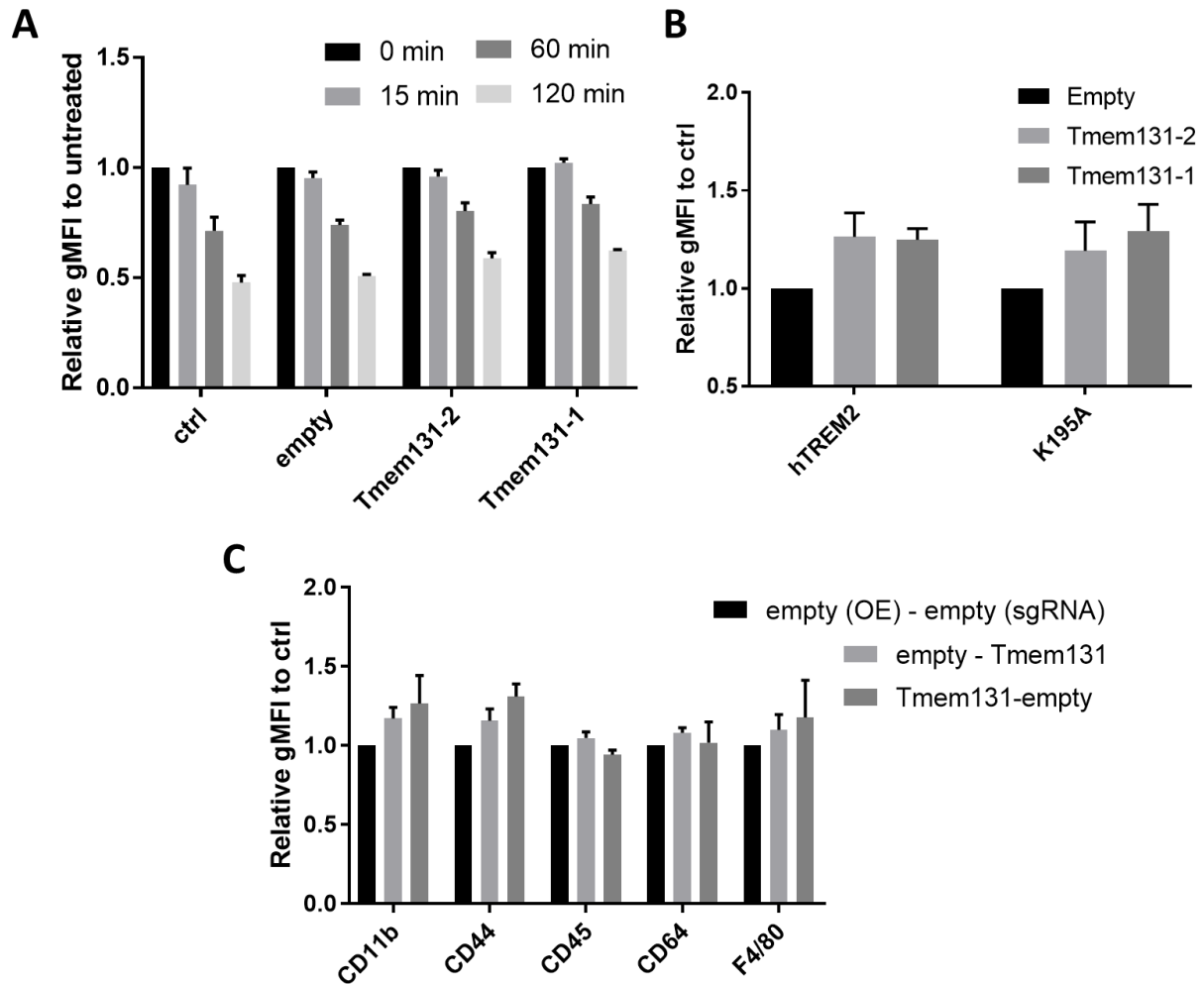


Figure 17. TMEM131 suppression of TREM2 does not involve faster degradation rate or require the intramembranous charge interactions of TREM2 and DAP12.

(A) Cycloheximide chase shows that surface TREM2 levels fall at a similar relative rate in control and TMEM131-KO BV2 cells. (B) TMEM131-KO increases expression of cleavage-resistant human TREM2 as well as the same construct with the intramembranous charged residue mutated. (C) Surface levels of other myeloid cell markers are not consistently altered by TMEM131 modulation, suggesting that the TREM2 effect is somewhat specific.

Chapter 5: Materials and methods

5.1 Methods for Chapter 2

Family cohort

The National Institute of Mental Health (NIMH) Alzheimer's Disease Genetics Initiative Study (1) originally ascertained for the study of genetic risk factors in AD with family-based methods, was used in the WGS analyses in this study. The basis for ascertainment in the NIMH collection was the existence of at least two affected individuals within a family, typically siblings. The complete NIMH study cohort contains a total of 1,536 subjects from 457 families. For the purpose of this analysis, only subjects of self-reported European ancestry were included, consisting of 1,376 participants (941 definitely affected and 404 definitely unaffected and the remainder could not be determined as definitely unaffected or definitely affected) from 410 families.

ADSP Whole-exome replication samples

The whole-exome variant calls (limited to SNVs only) were obtained from the Alzheimer's Disease Sequencing Project (ADSP) study (Study Accession: phs000572.v6.p4) by requesting accession authorization through dbGaP. The entire study data consists of whole exome sequencing data on 5096 cases 4965 controls, and an additional 853 (682 Cases [510 Non-Hispanic, 172 Hispanic]), and 171 Hispanic Control subjects from families that are multiply

affected with AD. For the purpose of this study, only the subjects with the self-reported Caucasian ethnicity were included in the replication analysis (n=10449).

Family-based Association Testing

Association analyses of the TREM2 variants in the NIMH-WGS dataset were performed using the family-based association test (FBAT (4) as implemented in PBAT (v3.6 (5)). To maximize statistical power, we tested AD affection status and age of onset jointly, using the multivariate extension of the FBAT-approach, FBAT-GEE (6). In order to minimize the multiple testing problems, we applied the weighted Bonferroni-testing strategy (7), which is an extension of the VanSteen algorithm (8).

Logistical Regression in Case-Control Whole-exome dataset

Logistical Regression using the binary affection status was performed using PLINK v1.90 (9). We used the additive model to assess allelic effects of SNPs given by the direction of the regression coefficient showing the effect of each extra minor allele, i.e. a positive regression coefficient means that the minor allele increases risk/phenotype mean.

Retroviral transduction.

Wild-type TREM2 and DAP12 were cloned into a pMX vector (10), and the QuikChange II XL Site-Directed Mutagenesis kit (Agilent) was used to generate variants. Lipofectamine 2000

(Thermo Fisher Scientific) was used to transfect Platinum E cells (Cell Biolabs) with 2.5 µg of each plasmid per 10 µL Lipofectamine 2000 to generate retroviral supernatants, per manufacturer instructions. After 48 hours and 72 hours, medium from 2B4 NFAT-GFP cultures was replaced with 0.45µm filtered fresh virus and the cells were spun for 1 hour minutes at 800 x g, after which additional medium was added. Successfully transduced cells were sorted after 1 week and again after 2 weeks based on TREM2 staining using a FACSAria II.

Quantitative RT-PCR

RNA was isolated from the indicated cells using TRIzol reagent (Thermo Fisher Scientific) according to manufacturer's instructions and concentration was determined using a Nanodrop (Thermo Fisher Scientific). Reverse transcription was performed using the SuperScript III First-Strand Synthesis System for RT-PCR (Invitrogen), and q-PCR was performed using iTaq Universal SYBR Green Supermix (Bio-Rad) on a Roche LightCycler 96. Primers used were as follows from 5' to 3': human TREM2 isoform 1 GCATCTCCAGGAGCCTCTTG and TGAGAAAGATGCAGGCCAGG; human TREM2 isoform 2 CGGGATGCTGGAGATCTCTG and TCTCAGCCCTGGAGATGCT; human DAP12 CCCGGAAACAGCGTATCACT and CGCTGTAGACATCCGACCTC; GAPDH CCTGGTATGACAACGAATTT and AGTGAGGGTCTCTCTCTTCC; HPRT GCAGTACAGCCCCAAAAT and AACAAAGTCTGGCCTGTATCCAA; Actb GGAGGGGGTTGAGGTGTT and TGTGCACTTTTATTGGTCTCAAG; murine DAP12 GAGTGACACTTTCCCAAGATGC and CCTTGACCTCGGGAGACCA; Spp1 CACTCCAATCGTCCCTACAGT and CTGGAAACTCCTAGACTTTGACC; Gpnmb

CATTCCCATCTCGAAGGTGAAA and AAATGGCAGAGTCGTTGAGGA; Cst7 GGAGCTGTACTTGCCGAGC and CATGGGTGTCAGAAGTTAGGC. The delta delta Ct method was used to calculate expression relative to HPRT, GAPDH, or Actb.

Flow cytometry

The indicated cells were washed in FACS buffer (2% bovine calf serum, 0.01% sodium azide in PBS), then stained with either isotype control, unconjugated anti-human TREM2 antibody (clones 29E3 and 10B11, hybridoma supernatant), or biotinylated anti-human TREM2 antibody (clone 21E10) in FACS buffer for 15 minutes on ice. After washing 3 times with FACS buffer, cells were incubated with PE-conjugated goat F(ab')₂ anti-mouse IgG1 (Southern Biotech cat. no. 1072-09, 1:20) or APC-conjugated streptavidin (Life Technologies cat. no. S868, 1:20) for 15 minutes on ice. Staining for myeloid cells was performed using BV421-anti-CD45 (30-F11, Biolegend, 1:200), FITC-anti-CD11b (M1/70, eBioscience, 1:200), and APC-anti-F4/80 (BM8, eBioscience, 1:100). After washing 3 times with FACS buffer, cells were resuspended in FACS buffer, propidium iodide was added (Sigma-Aldrich, final concentration 5µg/mL), and cells were read on a FACSCalibur. Cells were gated based on forward and side scatter and propidium iodide negativity.

Reporter assay

Phosphatidylcholine (Avanti, #840051P), phosphatidylserine (Avanti, #840032P), and sulfatides (Avanti, #131305P) were reconstituted in methanol, methanol, and chloroform :

methanol : water 2 : 1 : 0.1, respectively. For each experiment, two Nunc-Immuno MicroWell 96 well solid plates (Sigma) were coated with the purified lipid ligands phosphatidylcholine, phosphatidylserine, or sulfatide by diluting to the indicated concentration in methanol and adding 50 μ L of the resulting solution to each well, with each condition performed in duplicate. Plates were allowed to dry by evaporation, leaving the ligands coated on the well bottom. For human HDL (Millipore) and human LDL (Millipore), stock solution was diluted to the proper concentration in carbonate buffer (15mM Na₂CO₃, 35mM NaHCO₃, pH 9.6) and 50 μ L of the resulting solution was added to each well, with each condition performed in duplicate. The plates were transferred to 4°C overnight. The next day, solution was aspirated from each well, and each well was washed once with 150 μ L of PBS. For plate-bound antibody, goat (Fab')₂ anti-mouse IgG (Southern Biotech, cat no. 1012-01) was diluted 1:100 in carbonate buffer, and 50 μ L of the resulting solution was added to wells in triplicate. The plate was placed at 4°C for 12 hours. Then, solution was aspirated and each well was washed once with 150 μ L of PBS. 29E3 hybridoma supernatant was plated in each well at 4°C. After 12 hours, the supernatant was aspirated and wells were washed once with 150 μ L of PBS.

After preparation of the plate, 50,000 cells in 75 μ L of complete media were added to each well. After 12 hours, the cells were transferred to FACS tube and read on a FACSCalibur. Cells were gated based on forward and side scatter and propidium iodide negativity. The nontransduced control was used to draw the gate for GFP positivity, and this gate was used to determine the %GFP⁺ for each variant and ligand concentration. The average %GFP⁺ at the lowest two concentrations for each variant were assumed to be baseline activation, and this value was subtracted from the curve for each respective variant. The values for all concentrations were summed to approximate the area under the curve, which was used for analysis.

Mice

Trem2^{-/-} 5XFAD mice were generated as previously described (Wang et al. 2015). The CTD-2210D2 bacterial artificial chromosome (BAC) clone was purchased from Thermo Fisher, and the R47H polymorphism was introduced by recombination using the Quick and Easy BAC Modification Kit (Gene Bridges). The entire BAC was injected into the nucleus of fertilized eggs from C57BL/6 x CBA mice, and CV and R47H founders were obtained. The two lines selected for further work were subsequently backcrossed onto the C57BL/6 background for at least four generations (some done in the process of crossing to Trem2^{-/-} and 5XFAD mice, both of which are on a C57BL/6 background). All mice were bred and housed in specific pathogen free conditions. Animals were sacrificed between the ages of 245-260 days (8.5 months), with each experimental group containing both transgenic and non-transgenic mice.

Cell culture and biochemical assays

To obtain thioglycollate-elicited peritoneal macrophages, mice were injected intraperitoneally with 1 mL of 3% thioglycollate medium (Sigma, prepared in water and autoclaved), and cells were harvested by peritoneal lavage after 3 days. Cells were subsequently stained for flow cytometry. To prepare bone marrow-derived macrophages, femurs and tibias were removed and flushed with PBS. Cells were counted and plated at 2×10^6 cells/100 mm petri dish in RPMI supplemented with Glutamax, penicillin/streptomycin, nonessential amino acids, pyruvate, and 10% heat inactivated fetal bovine serum and 10% L-cell conditioned medium (LCCM) as a source of colony stimulating factor 1 (CSF1). Cells were cultured for 4-6 days before use. Human HDL (Millipore) was supplemented at a concentration of 50 $\mu\text{g/mL}$.

RAW264.7 cells were cultured on non-tissue culture treated 12-well plates in RPMI supplemented with Glutamax, penicillin/streptomycin, pyruvate, and 5% fetal bovine serum.

RAW264.7 cells were transduced with Cas9 overexpression lentivirus and transfected with plasmid expressing guide RNA against murine TREM2. TREM2-negative cells were sorted by FACS. lentiCas9-Blast and lentiGuide-Puro were gifts from Feng Zhang (Addgene plasmids # 52962, #52963, respectively). These TREM2-deficient RAW264.7 were retrovirally transduced with either CV or R47H driven under the CMV promoter and cells were sorted for hTREM2 expression by FACS. Cells were stimulated for 30 minutes or 2 hours with 10 ng/mL LPS (K12, Invivogen), 20 ng/mL recombinant TNF α (Peprotech), or 20 ng/mL recombinant IFN γ (Peprotech). For sorting Adam17-KO populations, cell were stimulated for 30 minutes with 10 ng/mL LPS and then stained for hTREM2.

Preparation of brain samples

Mice were anesthetized with ketamine/xylazine and perfused with ice-cold PBS containing 1 U/ml of heparin. Right brain hemispheres were fixed in 4% PFA overnight at 4°C rinsed in PBS and incubated overnight at 4°C in 30% sucrose before freezing in a 2:1 mixture of 30% sucrose and optimal cutting temperature compound. Serial 40 μ m coronal sections were cut on a cryo-sliding microtome. Cortices and hippocampi of the left-brain hemispheres were carefully dissected out and flash frozen for biochemical analysis. A portion of cortex was preserved in RNAlater (Ambion) until all samples were collected.

Confocal microscopy

Floating sections were blocked with 3% bovine serum albumin and 0.25% Triton X-100 in PBS, and then stained with anti-Iba-1 (rabbit polyclonal, Wako, 1:5000; or goat polyclonal, Abcam 1:1000), anti-human TREM2 ECD (goat polyclonal, R&D, 1:500), anti-human TREM2 C-terminus (D814C rabbit mAb, Cell Signaling, 1:500), anti-Spp1 (goat polyclonal, R&D, 1:500), anti-APP (22C11 mouse mAb, Millipore, 1:1000) and/or anti-NeuN (D3S3I rabbit mAb, Cell Signaling, 1:500) overnight at 4°C followed by staining with anti-rabbit IgG DyLight 549 (Vector, 1:2000), anti-goat IgG AlexaFluor-488 (Abcam, 1:2000), anti-rabbit IgG AlexaFluor-647 (goat polyclonal, Invitrogen, 1:1000), anti-goat IgG-biotin (donkey polyclonal, Invitrogen, 1:2000), streptavidin AlexaFluor-647 (Invitrogen, 1:2000), methoxy-X04 (Tocris, 3 µg/mL), and/or TO-PRO-3 iodide (Thermo-Fisher, 300 nM) for 1 hour at RT. All antibodies were used in blocking buffer, and between all incubations, sections were washed for ten minutes in PBS three times. Images were collected using a Nikon A1Rsi+ confocal microscope. 3D image segmentation of microglia, plaques, and neurons, and extraction of parameters were performed in Imaris 8.1 (Bitplane), and further processing was performed using automated scripts in Matlab (Mathworks). For detailed image analysis procedures, see Supplementary Methods.

Immunoblot

Samples were prepared from PBS-soluble or PBS-insoluble guanidine-soluble fractions of brain homogenates (as described above), or from cell lysates, by adding 1X NuPAGE LDS sample buffer (Invitrogen) and 10% β-mercaptoethanol and boiling for 5 minutes. Samples were run on NuPAGE 4-12% Bis-Tris pre-cast gels (Invitrogen), transferred to nitrocellulose

membranes, and blocked with 5% milk in PBS+0.05% Tween-20 (PBS-T) for 1 hour at room temperature. Membranes were incubated with in-house generated 29E3 anti-human TREM2 antibody (mouse IgG1, 4 µg/mL), anti-TACE/ADAM17 (rabbit polyclonal, Novus, 1:1000), or anti-pan-actin (rabbit polyclonal, Cell Signaling, 1:4000) in 0.5% milk/PBS-T overnight at 4°C, and incubated in HRP-conjugated anti-rabbit Ig (goat polyclonal, Southern, 1:1000) or HRP-conjugated anti-mouse IgG1 (goat polyclonal, Southern, 1:1000) at room temperature for 1 hour, with 3 washes of PBS-T between steps. Blots were detected by SuperSignal West Pico Chemiluminescent Substrate or SuperSignal West Femto Maximum Sensitivity Substrate (Thermo) with autoradiographic film. Developed films were scanned using an Epson Perfection V370 Photo scanner and analyzed using Image Studio Lite (LI-COR).

qRT-PCR and microarray analysis

For microarray analysis of sorted microglia, perfused brains were homogenized using the Neural Dissociation Kit (T) (Miltenyi) per manufacturer instructions. The homogenized tissue was run through a 70µm cell strainer and resuspended and centrifuged in 30% Percoll (GE). The resulting pellet was stained for CD11b and CD45, and CD11b+CD45+ cells were sorted using a FACSAriaII. RNA was extracted from sorted cells using the RNeasy Micro Plus kit (Qiagen) per manufacturer instructions and submitted for microarray analysis at the Genome Technology Access Center at Washington University. Samples were amplified using the Nugen Ovation Pico SL and run on the Affymetrix Gene 1.0 ST platform.

Statistics

Data in figures are presented as mean \pm SEM. Unless otherwise stated, statistical analysis was performed using Prism (GraphPad). Statistical analysis to compare the mean values for multiple groups was performed using a one-way or two-way ANOVA, as appropriate, with Holm-Sidak multiple comparisons testing.

5.2 Methods for Chapter 3

Mice

The generation of Trem2^{-/-} and Trem2^{-/-} 5XFAD mice has been described previously (Oakley et al., 2006; Turnbull et al., 2006; Wang et al., 2015). All mice were on a C57BL/6 background. Age and sex matched mice were used for all experiments; experimental cohorts of mice were cohoused from birth to control for the microbiota. For *in vivo* cyclocreatine treatment 10-week old mice were put on cyclocreatine-containing water, treatment was continued until mice reached 8 months of age (Santa Cruz SC-217964 S). Desired intake of cyclocreatine was approximately 0.28 mg/g of body weight/day, which is approximately the same as the standard creatine dose used in humans of 285 mg/kg of body weight/day¹⁶⁴. Cyclocreatine was administered in drinking water at a final concentration of 2.33 mg/ml. Bhlhe40-EGFP and Bhlhe40-deficient mice have previously been described¹⁶⁵. The Institutional Animal Care and Use Committee at Washington University in St. Louis approved all protocols used in this study.

Cell culture and biochemical assays

To prepare bone marrow-derived macrophages, femurs and tibias were removed and flushed with PBS. Cells were counted and plated at 2.5×10^6 cells/100 mm petri dish in RPMI supplemented with Glutamax, penicillin/streptomycin, nonessential amino acids, pyruvate, and 10% heat inactivated fetal bovine serum (complete RPMI) and 10% L-cell conditioned medium (LCCM). Cells were cultured for 4-5 days before use. ATP concentrations were determined with an ATP Determination Kit (Invitrogen).

Microglia sorting

Microglia were isolated from the indicated animals as previously described (Wang et al., 2015). CD45⁺, CD11b⁺, F4/80⁺ (Biolegend Cat. Number 103134, eBioscience Cat. Numbers 11-0112 and 17-4801) cells in the brain were fluorescence-activated cell-sorted (FACS) directly into RLT-plus lysis buffer for microarray or 2% FBS in PBS for TEM or immunoblot lysates. For microarray RNA extraction was performed using a RNeasy micro kit (QIAGEN). Microarray hybridization (Affymetrix MoGene 1.0 ST array) and data processing were performed at the Washington University Genome Center.

Immunoblotting

BMDM or microglia were lysed in RIPA buffer (50 mM Tris, 150mM NaCl, 1% SDS, and 1% Triton X100) containing PMSF, leupeptin, activated sodium orthovanadate, apoprotinin, and phosphatase inhibitor cocktail 3 (Sigma Aldrich Cat. Number P0044). Lysates were flash frozen on dry ice and stored at -80o C until use. Lysates were thawed and 4x LDS running buffer

and 10% β -mercaptoethanol were added. Lysates were heated to 95°C for 10 minutes and run on either a 15 % polyacrylamide gel with a 4% stacking gel, a 12% bis-tris gel (Nupage), or a 4-12% bis-tris gel (Nupage). Proteins were transferred to nitrocellulose and blocked for 1 hour at RT in 5% milk in Tris buffered saline with 0.05% Tween 20 (TBST). Membranes were incubated in primary antibody overnight at 4°C (Supplemental Table 2). Membranes were subsequently washed and incubated in Leinco anti-rabbit HRP for 1 hour at RT, washed, and developed using either SuperSignal West Pico Chemiluminescent Substrate or a combination of SuperSignal West Pico Chemiluminescent Substrate and SuperSignal West Femto Chemiluminescent Substrate.

Metabolism assays

For real-time analysis of extracellular acidification rates (ECAR) macrophages were analyzed using an XF96 Extracellular Flux Analyzer (Agilent Technologies). Cells were incubated overnight in complete RPMI in the indicated concentration of LCCM with or without cyclocreatine (10 mM). Measurements were taken under basal conditions and following the sequential addition of 1 μ M oligomycin and 1.5 μ M fluoro-carbonyl cyanide phenylhydrazone (FCCP) (purchased from Sigma-Aldrich).

Transmission electron microscopy

For ultrastructural analyses, cells were fixed in 2% paraformaldehyde/2.5% glutaraldehyde in 100 mM sodium cacodylate buffer, pH 7.2 for 1 hr at RT (Polysciences Inc.,

Warrington, PA). Samples were washed in sodium cacodylate buffer and postfixed in 1% osmium tetroxide for 1 hr (Polysciences Inc.). Samples were then rinsed extensively in deionized water prior to en bloc staining with 1% aqueous uranyl acetate for 1 hr (Ted Pella Inc., Redding, CA). Following several rinses in dH₂O, samples were dehydrated in a graded series of ethanol and embedded in Eponate 12 resin (Ted Pella Inc.). Sections of 95 nm were cut with a Leica Ultracut UCT ultramicrotome (Leica Microsystems Inc., Bannockburn, IL), stained with uranyl acetate and lead citrate, and viewed on a JEOL 1200 EX transmission electron microscope (JEOL USA Inc., Peabody, MA) equipped with an AMT 8 megapixel digital camera and AMT Image Capture Engine V602 software (Advanced Microscopy Techniques, Woburn, MA). For quantitation of multivesicular/multilamellar structures, 30 cells that were cross-sectioned through the nucleus (indicating cross-section through the middle of cell) were randomly chosen, and images of each cell were taken at 6,000X and 20,000X magnification. The cross-sectional area of each of the multivesicular structures were determined using Image J 1.38g (National Institutes of Health, USA, customized for AMT images). Data is expressed as the 1) total number of a multivesicular/multilammelar structures per cross sectional area of cytosol and 2) the total cross-sectional area of multivesicular/multilamellar structures per area of cytosol.

Preparation of brain samples and confocal microscopy

Confocal microscopy analysis was performed as previously described (Wang et al., 2015). Briefly, mice were anesthetized with ketamine/xylazine and perfused with ice-cold PBS containing 1 U/ml of heparin. Brains were fixed in 4% PFA overnight at 4o C rinsed in PBS and incubated overnight at 4o C in 30% sucrose before freezing in a 2:1 mixture of 30% sucrose and

optimal cutting temperature compound. Serial 40 μm coronal sections were cut on a cryo-sliding microtome. Floating sections from 1.1 mm Bregma to 0.8 mm Bregma for cortical imaging were stained with Iba-1 (Wako Chemicals Cat. Number 019-19741) overnight at 40 C followed by staining with anti-rabbit IgG DyLight 549 (Vector Laboratories Cat. Number DI-1549) and methoxy-X04 (Tocris Cat. Number 4920) for 1 hour at RT. Images were collected using a Nikon A1Rsi+ confocal microscope. Images were then processed with Imaris 7.7 (Bitplane).

Microglia clustering analysis

Positions of microglia and positions and volumes of plaques within z-stacks were derived from analysis in Imaris, and microglia-plaque association was determined using automated scripts in Matlab. Briefly, each plaque in the z-stack was modeled as an idealized sphere with the same volume and center of mass. Microglia density within 15 or 20 μm of the plaque surface was determined by isolating the voxels of the image that fall within 15 or 20 μm of the edge of the idealized plaque. The number of microglia contained in these voxels was divided by the total volume of those voxels to obtain density for a single plaque. Densities of all plaques in a z-stack were averaged together, and the resulting values were averaged together for all z-stacks corresponding to a single animal.

Reporter cell assay

The 2B4 T cell hybridoma cell line was retrovirally transduced with an NFAT-GFP reporter construct, and TREM2 reporter cells were generated by a second retroviral transduction

with a TREM2 overexpression construct and selected by puromycin resistance, as previously described (Wang et al., 2015). Cells were cultured routinely in complete media (10% FBS in RPMI-1640 supplemented with sodium pyruvate, GlutaMAX, and penicillin/streptomycin). For serum starvation, cells were plated at a density of 25,000 cells/well in a 96-well plate in either complete media or RPMI-1640 in the presence of 20% anti-TREM2 hybridoma supernatant (clone M178, generated in house) or 20% isotype control hybridoma supernatant (Wang et al., 2015). After 16 hours, the percent of GFP+ cells among live cells was measured by flow cytometry.

5.3 Methods for Chapter 4

Library preparation and screening

BV2 cells were transduced with Cas9 overexpression lentivirus lentiCas9-Blast, selected by blasticidin treatment to obtain BV2-Cas9 cells. These cells were subsequently transduced with lentiGuide-Puro Asiago library subpools 1, 2, 5, or 6¹⁶³ and selected by puromycin treatment to generate 4 independent genome-wide knockout libraries. Each library was divided into two batches as technical replicates. Three sequential sorts were performed for each library by sorting the top or bottom 20% of TREM2-expressing cells multiple times with two days of equilibration in culture between sorts. Specifically, TREM2-high cells were sorted again for the top 20% to generate TREM2-high-high cells, while TREM2-low cells were sorted again for the bottom 20% to generate TREM2-low-low cells, etc. After each sort, a portion of the cells was harvested for DNA extraction, such that we assayed all combinations of different libraries and different numbers of sorts. A fraction of cells was maintained in culture for the same duration of

time without sorting to serve as a control. These samples were submitted to the Genetic Perturbation Platform at the Broad Institute for amplification and deep sequencing.

Cell culture

All BV2-derived cell lines were cultured in 5% FBS in RPMI supplemented with GlutaMAX, sodium pyruvate, and penicillin/streptomycin. BV2-Trem2-KO cells were previously generated by CRISPR-Cas9 followed by sorting of TREM2-negative cells. These TREM2-deficient BV2 were retrovirally transduced with pMX vectors carrying cleavage-resistant hTREM2 (hTREM2-CD8, residues 133-174 of hTREM2 replaced with the sequence TTTTAPRPPTPAPTIASQPLSLRPEACRPAAGGAVHTRGLDFACD from CD8 stem region) or hTREM-CD8 with an additional point mutation (K186A), followed by IRES and human DAP12. Lentivirally-mediated CRISPR-Cas9 knockout was performed by cloning the appropriate sgRNA sequence into either the lentiGuide-Puro or lentiCRISPRv2-Blast vectors. TMEM131 was cloned from cDNA derived from mouse brain, and the obtained sequence corresponded to the predicted isoform X2. This fragment was inserted into the pMX-IRES-puro vector with a C-terminal 3XFLAG tag. Cycloheximide was used at a concentration of 25 µg/mL. GM6001 was used at a concentration of 10 µg/mL.

Flow cytometry

Cells were washed in FACS buffer (2% bovine calf serum, 0.01% sodium azide in PBS), then stained with either isotype control, unconjugated anti-human TREM2 antibody (clones

29E3 or 21E10, hybridoma supernatant), or in FACS buffer for 15 minutes on ice. After washing 3 times with FACS buffer, cells were incubated with PE-conjugated goat F(ab')₂ anti-mouse IgG1 (Southern Biotech cat. no. 1072-09, 1:20) or PE-conjugated goat anti-rat IgG (Southern Biotech cat. no. 3030-09) for 15 minutes on ice. Staining for other myeloid markers was performed using FITC-anti-CD44 (eBioscience, 1:200), PE-anti-CD64 (eBioscience, 1:200), FITC-anti-CD45 (30-F11, eBioscience, 1:200), FITC-anti-CD11b (M1/70, eBioscience, 1:200), and PE-anti-F4/80 (BM8, eBioscience, 1:100). After washing 3 times with FACS buffer, cells were resuspended in FACS buffer, propidium iodide was added (Sigma-Aldrich, final concentration 5µg/mL), and cells were read on a FACSCalibur. Cells were gated based on forward and side scatter.

References

1. Heneka, M. T., Golenbock, D. T. & Latz, E. Innate immunity in Alzheimer's disease. *Nat. Immunol.* **16**, 229–236 (2015).
2. Cohen, M. *et al.* Chronic exposure to TGF β 1 regulates myeloid cell inflammatory response in an IRF7-dependent manner. *EMBO J.* **33**, 2906–21 (2014).
3. Colonna, M. & Butovsky, O. Microglia Function in the Central Nervous System During Health and Neurodegeneration. *Annu. Rev. Immunol.* **35**, 441–468 (2017).
4. Heppner, F. L., Ransohoff, R. M. & Becher, B. Immune attack: The role of inflammation in Alzheimer disease. *Nature Reviews Neuroscience* **16**, 358–372 (2015).
5. Prinz, M., Priller, J., Sisodia, S. S. & Ransohoff, R. M. Heterogeneity of CNS myeloid cells and their roles in neurodegeneration. *Nat. Neurosci.* **14**, 1227–1235 (2011).
6. Ginhoux, F. *et al.* Fate Mapping Analysis Reveals That Adult Microglia Derive from Primitive Macrophages. *Science (80-.).* **330**, (2010).
7. Ajami, B., Bennett, J. L., Krieger, C., Tetzlaff, W. & Rossi, F. M. V. Local self-renewal can sustain CNS microglia maintenance and function throughout adult life. *Nat. Neurosci.* **10**, 1538–1543 (2007).
8. Tay, T. L. *et al.* A new fate mapping system reveals context-dependent random or clonal expansion of microglia. *Nat. Neurosci.* **20**, (2017).
9. Askew, K. *et al.* Coupled Proliferation and Apoptosis Maintain the Rapid Turnover of Microglia in the Adult Brain. *Cell Rep.* **18**, 391–405 (2017).
10. Zhang, D. E., Hetherington, C. J., Chen, H. M. & Tenen, D. G. The macrophage transcription factor PU.1 directs tissue-specific expression of the macrophage colony-stimulating factor receptor. *Mol. Cell. Biol.* **14**, 373–81 (1994).
11. Kierdorf, K. *et al.* Microglia emerge from erythromyeloid precursors via Pu.1- and Irf8-dependent pathways. *Nat. Neurosci.* **16**, 273–80 (2013).
12. Buttgereit, A. *et al.* Sall1 is a transcriptional regulator defining microglia identity and function. *Nat. Immunol.* **17**, 1397–1406 (2016).
13. Erny, D. *et al.* Host microbiota constantly control maturation and function of microglia in the CNS. *Nat. Neurosci.* **18**, 965–77 (2015).
14. Thion, M. S. *et al.* Microbiome Influences Prenatal and Adult Microglia in a Sex-Specific Manner. *Cell* **172**, 500–516.e16 (2018).

15. Gautier, E. L. *et al.* Gene-expression profiles and transcriptional regulatory pathways that underlie the identity and diversity of mouse tissue macrophages. *Nat. Immunol.* **13**, 1118–28 (2012).
16. Galatro, T. F. *et al.* Transcriptomic analysis of purified human cortical microglia reveals age-associated changes. *Nat. Neurosci.* **20**, 1162–1171 (2017).
17. Gosselin, D. *et al.* An environment-dependent transcriptional network specifies human microglia identity. *Science (80-.).* **356**, 1248–1259 (2017).
18. Butovsky, O. *et al.* Identification of a unique TGF- β -dependent molecular and functional signature in microglia. *Nat. Neurosci.* **17**, 131–43 (2014).
19. Bohlen, C. J. *et al.* Diverse Requirements for Microglial Survival, Specification, and Function Revealed by Defined-Medium Cultures. *Neuron* **94**, 759–773.e8 (2017).
20. Abud, E. M. *et al.* iPSC-Derived Human Microglia-like Cells to Study Neurological Diseases. *Neuron* **94**, 278–293.e9 (2017).
21. Haenseler, W. *et al.* A Highly Efficient Human Pluripotent Stem Cell Microglia Model Displays a Neuronal-Co-culture-Specific Expression Profile and Inflammatory Response. *Stem Cell Reports* **8**, 1727–1742 (2017).
22. Pandya, H. *et al.* Differentiation of human and murine induced pluripotent stem cells to microglia-like cells. *Nat. Neurosci.* **20**, 753–759 (2017).
23. Bennett, F. C. *et al.* A Combination of Ontogeny and CNS Environment Establishes Microglial Identity. *Neuron* **98**, 1170–1183.e8 (2018).
24. Cronk, J. C. *et al.* Peripherally derived macrophages can engraft the brain independent of irradiation and maintain an identity distinct from microglia. *J. Exp. Med.* jem.20180247 (2018). doi:10.1084/jem.20180247
25. Grabert, K. *et al.* Microglial brain region-dependent diversity and selective regional sensitivities to aging. *Nat. Neurosci.* **19**, 504–16 (2016).
26. Itagaki, S., McGeer, P. L., Akiyama, H., Zhu, S. & Selkoe, D. Relationship of microglia and astrocytes to amyloid deposits of Alzheimer disease. *J. Neuroimmunol.* **24**, 173–82 (1989).
27. Efthymiou, A. G. & Goate, A. M. Late onset Alzheimer’s disease genetics implicates microglial pathways in disease risk. *Mol. Neurodegener.* **12**, 43 (2017).
28. Zhang, B. *et al.* Integrated Systems Approach Identifies Genetic Nodes and Networks in Late-Onset Alzheimer’s Disease. *Cell* **153**, 707–720 (2013).
29. Huang, K. *et al.* A common haplotype lowers PU.1 expression in myeloid cells and delays onset of Alzheimer’s disease. *Nat. Neurosci.* **20**, 1052–1061 (2017).

30. Soreq, L. *et al.* Major Shifts in Glial Regional Identity Are a Transcriptional Hallmark of Human Brain Aging. *Cell Rep.* **18**, 557–570 (2017).
31. McGeer, P. L., Itagaki, S., Boyes, B. E. & McGeer, E. G. Reactive microglia are positive for HLA-DR in the substantia nigra of Parkinson's and Alzheimer's disease brains. *Neurology* **38**, 1285–91 (1988).
32. Sapp, E. *et al.* Early and Progressive Accumulation of Reactive Microglia in the Huntington Disease Brain. *J. Neuropathol. Exp. Neurol.* **60**, 161–172 (2001).
33. Pavese, N. *et al.* Microglial activation correlates with severity in Huntington disease: a clinical and PET study. *Neurology* **66**, 1638–43 (2006).
34. Oakley, H. *et al.* Intraneuronal beta-Amyloid Aggregates, Neurodegeneration, and Neuron Loss in Transgenic Mice with Five Familial Alzheimer's Disease Mutations: Potential Factors in Amyloid Plaque Formation. *J. Neurosci.* **26**, 10129–10140 (2006).
35. Yoshiyama, Y. *et al.* Synapse Loss and Microglial Activation Precede Tangles in a P301S Tauopathy Mouse Model. *Neuron* **53**, 337–351 (2007).
36. Francis, J. W., Von Visger, J., Markelonis, G. J. & Oh, T. H. Neuroglial responses to the dopaminergic neurotoxicant 1-methyl-4-phenyl-1,2,3,6-tetrahydropyridine in mouse striatum. *Neurotoxicol. Teratol.* **17**, 7–12 (1995).
37. Hall, E. D., Oostveen, J. A. & Gurney, M. E. Relationship of microglial and astrocytic activation to disease onset and progression in a transgenic model of familial ALS. *Glia* **23**, 249–56 (1998).
38. Deczkowska, A. *et al.* Disease-Associated Microglia: A Universal Immune Sensor of Neurodegeneration. *Cell* **173**, 1073–1081 (2018).
39. Orre, M. *et al.* Isolation of glia from Alzheimer's mice reveals inflammation and dysfunction. *Neurobiol. Aging* **35**, 2746–2760 (2014).
40. Wang, Y. *et al.* TREM2 lipid sensing sustains the microglial response in an Alzheimer's disease model. *Cell* **160**, 1061–1071 (2015).
41. Kamphuis, W., Kooijman, L., Schetters, S., Orre, M. & Hol, E. M. Transcriptional profiling of CD11c-positive microglia accumulating around amyloid plaques in a mouse model for Alzheimer's disease. *Biochim. Biophys. Acta - Mol. Basis Dis.* **1862**, 1847–1860 (2016).
42. Friedman, B. A. *et al.* Diverse Brain Myeloid Expression Profiles Reveal Distinct Microglial Activation States and Aspects of Alzheimer's Disease Not Evident in Mouse Models. *Cell Rep.* **22**, 832–847 (2018).
43. Chiu, I. M. *et al.* A neurodegeneration-specific gene-expression signature of acutely isolated microglia from an amyotrophic lateral sclerosis mouse model. *Cell Rep.* **4**, 385–

- 401 (2013).
44. Mathys, H. *et al.* Temporal Tracking of Microglia Activation in Neurodegeneration at Single-Cell Resolution. *Cell Rep.* **21**, 366–380 (2017).
 45. Ajami, B. *et al.* Single-cell mass cytometry reveals distinct populations of brain myeloid cells in mouse neuroinflammation and neurodegeneration models. *Nat. Neurosci.* **21**, 541–551 (2018).
 46. Mrdjen, D. *et al.* High-Dimensional Single-Cell Mapping of Central Nervous System Immune Cells Reveals Distinct Myeloid Subsets in Health, Aging, and Disease. *Immunity* **48**, 380–395.e6 (2018).
 47. Holtman, I. R. *et al.* Induction of a common microglia gene expression signature by aging and neurodegenerative conditions: a co-expression meta-analysis. *Acta Neuropathol. Commun.* **3**, 31 (2015).
 48. Keren-Shaul, H. *et al.* A Unique Microglia Type Associated with Restricting Development of Alzheimer’s Disease. *Cell* **169**, 1276–1290.e17 (2017).
 49. Rangaraju, S. *et al.* Identification and therapeutic modulation of a pro-inflammatory subset of disease-associated-microglia in Alzheimer’s disease. *Mol. Neurodegener.* **13**, 24 (2018).
 50. Poliani, P. L. *et al.* TREM2 sustains microglial expansion during aging and response to demyelination. *J. Clin. Invest.* **125**, 2161–2170 (2015).
 51. Raj, D. D. A. *et al.* Priming of microglia in a DNA-repair deficient model of accelerated aging. *Neurobiol. Aging* **35**, 2147–2160 (2014).
 52. Krasemann, S. *et al.* The TREM2-APOE Pathway Drives the Transcriptional Phenotype of Dysfunctional Microglia in Neurodegenerative Diseases. *Immunity* **47**, 566–581.e9 (2017).
 53. Wlodarczyk, A. *et al.* A novel microglial subset plays a key role in myelinogenesis in developing brain. *EMBO J.* **36**, 3292–3308 (2017).
 54. Leyns, C. E. G. *et al.* TREM2 deficiency attenuates neuroinflammation and protects against neurodegeneration in a mouse model of tauopathy. *Proc. Natl. Acad. Sci.* **114**, 11524–11529 (2017).
 55. Kang, S. S. *et al.* Behavioral and transcriptomic analysis of Trem2-null mice: not all knockout mice are created equal. *Hum. Mol. Genet.* **27**, 211–223 (2018).
 56. Turnbull, I. R. *et al.* Cutting edge: TREM-2 attenuates macrophage activation. *J. Immunol.* **177**, 3520–4 (2006).
 57. Zheng, H. *et al.* TREM2 promotes microglial survival by activating Wnt/#-catenin

- pathway. (2017). doi:10.1523/JNEUROSCI.2459-16.2017
58. Zhu, C. *et al.* Triggering receptor expressed on myeloid cells-2 is involved in prion-induced microglial activation but does not contribute to prion pathogenesis in mouse brains. *Neurobiol. Aging* **36**, 1994–2003 (2015).
 59. Ulrich, J. D. *et al.* ApoE facilitates the microglial response to amyloid plaque pathology. *J. Exp. Med.* jem.20171265 (2018). doi:10.1084/jem.20171265
 60. Yeh, F. L., Wang, Y., Tom, I., Gonzalez, L. C. & Sheng, M. TREM2 Binds to Apolipoproteins, Including APOE and CLU/APOJ, and Thereby Facilitates Uptake of Amyloid-Beta by Microglia. *Neuron* **91**, 328–340 (2016).
 61. Bailey, C. C., DeVaux, L. B. & Farzan, M. The Triggering Receptor Expressed on Myeloid Cells 2 Binds Apolipoprotein E. *J. Biol. Chem.* **290**, 26033–42 (2015).
 62. Atagi, Y. *et al.* Apolipoprotein E Is a Ligand for Triggering Receptor Expressed on Myeloid Cells 2 (TREM2). *J. Biol. Chem.* **290**, 26043–26050 (2015).
 63. Otero, K. *et al.* Macrophage colony-stimulating factor induces the proliferation and survival of macrophages via a pathway involving DAP12 and β -catenin. *Nat. Immunol.* **10**, 734–743 (2009).
 64. Weber, G. F., Ashkar, S., Glimcher, M. J. & Cantor, H. Receptor-ligand interaction between CD44 and osteopontin (Eta-1). *Science* **271**, 509–12 (1996).
 65. Butovsky, O. *et al.* Targeting miR-155 restores abnormal microglia and attenuates disease in SOD1 mice. *Ann. Neurol.* **77**, 75–99 (2015).
 66. Hardy, J. & Selkoe, D. J. The amyloid hypothesis of Alzheimer’s disease: progress and problems on the road to therapeutics. *Science* **297**, 353–6 (2002).
 67. Hardy, J. Amyloid, the presenilins and Alzheimer’s disease. *Trends Neurosci.* **20**, 154–159 (1997).
 68. Hickman, S. E., Allison, E. K. & El Khoury, J. Microglial dysfunction and defective beta-amyloid clearance pathways in aging Alzheimer’s disease mice. *J. Neurosci.* **28**, 8354–60 (2008).
 69. Mawuenyega, K. G. *et al.* Decreased clearance of CNS beta-amyloid in Alzheimer’s disease. *Science* **330**, 1774 (2010).
 70. Lee, C. Y. D. & Landreth, G. E. The role of microglia in amyloid clearance from the AD brain. *J. Neural Transm.* **117**, 949–60 (2010).
 71. Bates, K. A. *et al.* Clearance mechanisms of Alzheimer’s amyloid- β peptide: implications for therapeutic design and diagnostic tests. *Mol. Psychiatry* **14**, 469–486 (2009).

72. Baranello, R. J. *et al.* Amyloid-beta protein clearance and degradation (ABCD) pathways and their role in Alzheimer's disease. *Curr. Alzheimer Res.* **12**, 32–46 (2015).
73. Liu, S. *et al.* TLR2 Is a Primary Receptor for Alzheimer's Amyloid Peptide To Trigger Neuroinflammatory Activation. *J. Immunol.* **188**, 1098–1107 (2012).
74. El Khoury, J. B. *et al.* CD36 mediates the innate host response to beta-amyloid. *J. Exp. Med.* **197**, 1657–1666 (2003).
75. Stewart, C. R. *et al.* CD36 ligands promote sterile inflammation through assembly of a Toll-like receptor 4 and 6 heterodimer. *Nat. Immunol.* **11**, 155–161 (2010).
76. Prokop, S. *et al.* Impact of peripheral myeloid cells on amyloid- β pathology in Alzheimer's disease-like mice. *J. Exp. Med.* **212**, 1811–8 (2015).
77. Varvel, N. H. *et al.* Replacement of brain-resident myeloid cells does not alter cerebral amyloid- β deposition in mouse models of Alzheimer's disease. *J. Exp. Med.* **212**, 1803–9 (2015).
78. Spangenberg, E. E. *et al.* Eliminating microglia in Alzheimer's mice prevents neuronal loss without modulating amyloid- β pathology. *Brain* **139**, 1265–1281 (2016).
79. Dagher, N. N. *et al.* Colony-stimulating factor 1 receptor inhibition prevents microglial plaque association and improves cognition in 3xTg-AD mice. *J. Neuroinflammation* **12**, 139 (2015).
80. Sosna, J. *et al.* Early long-term administration of the CSF1R inhibitor PLX3397 ablates microglia and reduces accumulation of intraneuronal amyloid, neuritic plaque deposition and pre-fibrillar oligomers in 5XFAD mouse model of Alzheimer's disease. *Mol. Neurodegener.* **13**, 11 (2018).
81. Chakrabarty, P. *et al.* IFN- γ Promotes Complement Expression and Attenuates Amyloid Plaque Deposition in Amyloid β Precursor Protein Transgenic Mice. *J. Immunol.* **184**, (2010).
82. Chakrabarty, P. *et al.* Massive gliosis induced by interleukin-6 suppresses A β deposition in vivo: evidence against inflammation as a driving force for amyloid deposition. *FASEB J.* **24**, 548–559 (2010).
83. Chakrabarty, P., Herring, A., Ceballos-Diaz, C., Das, P. & Golde, T. E. Hippocampal expression of murine TNF α results in attenuation of amyloid deposition in vivo. *Mol. Neurodegener.* **6**, 16 (2011).
84. Guillot-Sestier, M.-V. *et al.* Il10 Deficiency Rebalances Innate Immunity to Mitigate Alzheimer-Like Pathology. *Neuron* **85**, 534–548 (2015).
85. Chakrabarty, P. *et al.* IL-10 Alters Immunoproteostasis in APP Mice, Increasing Plaque Burden and Worsening Cognitive Behavior. *Neuron* **85**, 519–533 (2015).

86. Sevigny, J. *et al.* The antibody aducanumab reduces A β plaques in Alzheimer's disease. *Nature* **537**, 50–56 (2016).
87. Leinenga, G. & Götz, J. Scanning ultrasound removes amyloid- β and restores memory in an Alzheimer's disease mouse model. *Sci. Transl. Med.* **7**, 278ra33 (2015).
88. Iaccarino, H. F. *et al.* Gamma frequency entrainment attenuates amyloid load and modifies microglia. *Nature* **540**, 230–235 (2016).
89. Yuan, P. *et al.* TREM2 Haplodeficiency in Mice and Humans Impairs the Microglia Barrier Function Leading to Decreased Amyloid Compaction and Severe Axonal Dystrophy. *Neuron* **90**, 724–739 (2016).
90. Stevens, B. *et al.* The Classical Complement Cascade Mediates CNS Synapse Elimination. *Cell* **131**, 1164–1178 (2007).
91. Stephan, A. H., Barres, B. A. & Stevens, B. The Complement System: An Unexpected Role in Synaptic Pruning During Development and Disease. *Annu. Rev. Neurosci.* **35**, 369–389 (2012).
92. Schafer, D. P. *et al.* Microglia sculpt postnatal neural circuits in an activity and complement-dependent manner. *Neuron* **74**, 691–705 (2012).
93. Harrison, J. K. *et al.* Role for neuronally derived fractalkine in mediating interactions between neurons and CX3CR1-expressing microglia. *Proc. Natl. Acad. Sci.* **95**, 10896–10901 (1998).
94. Hoshiko, M., Arnoux, I., Avignone, E., Yamamoto, N. & Audinat, E. Deficiency of the microglial receptor CX3CR1 impairs postnatal functional development of thalamocortical synapses in the barrel cortex. *J. Neurosci.* **32**, 15106–11 (2012).
95. Hong, S. *et al.* Complement and Microglia Mediate Early Synapse Loss in Alzheimer Mouse Models. *Science* **33**, 395–401 (2015).
96. Shi, Q. *et al.* Complement C3-Deficient Mice Fail to Display Age-Related Hippocampal Decline. *J. Neurosci.* **35**, 13029–42 (2015).
97. Singhrao, S. ., Neal, J. ., Morgan, B. . & Gasque, P. Increased Complement Biosynthesis By Microglia and Complement Activation on Neurons in Huntington's Disease. *Exp. Neurol.* **159**, 362–376 (1999).
98. Acharya, M. M. *et al.* Elimination of microglia improves cognitive function following cranial irradiation. *Sci. Rep.* **6**, 31545 (2016).
99. Haure-Mirande, J.-V. *et al.* Deficiency of TYROBP, an adapter protein for TREM2 and CR3 receptors, is neuroprotective in a mouse model of early Alzheimer's pathology. *Acta Neuropathol.* **134**, 769–788 (2017).

100. Fourgeaud, L. *et al.* TAM receptors regulate multiple features of microglial physiology. *Nature* **532**, 240–244 (2016).
101. Wong, K. *et al.* Mice deficient in NRROS show abnormal microglial development and neurological disorders. *Nat. Immunol.* **18**, 633–641 (2017).
102. Mass, E. *et al.* A somatic mutation in erythro-myeloid progenitors causes neurodegenerative disease. *Nature* **549**, 389–393 (2017).
103. Brionne, T. C., Tesseur, I., Masliah, E. & Wyss-Coray, T. Loss of TGF-beta 1 leads to increased neuronal cell death and microgliosis in mouse brain. *Neuron* **40**, 1133–45 (2003).
104. Paloneva, J. *et al.* Mutations in Two Genes Encoding Different Subunits of a Receptor Signaling Complex Result in an Identical Disease Phenotype. *Am. J. Hum. Genet.* **71**, 656–662 (2002).
105. Cella, M. *et al.* Impaired differentiation of osteoclasts in TREM-2-deficient individuals. *J. Exp. Med.* **198**, 645–51 (2003).
106. Xing, J., Titus, A. R. & Humphrey, M. B. The TREM2-DAP12 signaling pathway in Nasu-Hakola disease: a molecular genetics perspective. *Res. reports Biochem.* **5**, 89–100 (2015).
107. Cantoni, C. *et al.* TREM2 regulates microglial cell activation in response to demyelination in vivo. *Acta Neuropathol.* **129**, 429–447 (2015).
108. Nicholson, A. M. *et al.* CSF1R mutations link POLD and HDLS as a single disease entity. *Neurology* **80**, 1033–1040 (2013).
109. Pridans, C., Sauter, K. A., Baer, K., Kissel, H. & Hume, D. A. CSF1R mutations in hereditary diffuse leukoencephalopathy with spheroids are loss of function. *Sci. Rep.* **3**, 3013 (2013).
110. Rademakers, R. *et al.* Mutations in the colony stimulating factor 1 receptor (CSF1R) gene cause hereditary diffuse leukoencephalopathy with spheroids. *Nat. Genet.* **44**, 200–205 (2012).
111. Dai, X.-M. *et al.* Targeted disruption of the mouse colony-stimulating factor 1 receptor gene results in osteopetrosis, mononuclear phagocyte deficiency, increased primitive progenitor cell frequencies, and reproductive defects. *Blood* **99**, 111–20 (2002).
112. Erlich, B., Zhu, L., Etgen, A. M., Dobrenis, K. & Pollard, J. W. Absence of Colony Stimulation Factor-1 Receptor Results in Loss of Microglia, Disrupted Brain Development and Olfactory Deficits. *PLoS One* **6**, e26317 (2011).
113. Forabosco, P. *et al.* Insights into TREM2 biology by network analysis of human brain gene expression data. *Neurobiol. Aging* **34**, 2699–2714 (2013).

114. Gjoneska, E. *et al.* Conserved epigenomic signals in mice and humans reveal immune basis of Alzheimer's disease. *Nature* **518**, 365–369 (2015).
115. Lambert, J.-C. *et al.* Genome-wide association study identifies variants at CLU and CR1 associated with Alzheimer's disease. *Nat. Genet.* **41**, 1094–9 (2009).
116. Hollingworth, P. *et al.* Common variants at ABCA7, MS4A6A/MS4A4E, EPHA1, CD33 and CD2AP are associated with Alzheimer's disease. *Nat. Genet.* **43**, 429–435 (2011).
117. Lambert, J. C. *et al.* Meta-analysis of 74,046 individuals identifies 11 new susceptibility loci for Alzheimer's disease. *Nat. Genet.* **45**, 1452–8 (2013).
118. Griciuc, A. *et al.* Alzheimer's Disease Risk Gene CD33 Inhibits Microglial Uptake of Amyloid Beta. *Neuron* **78**, 631–643 (2013).
119. Guerreiro, R. *et al.* TREM2 Variants in Alzheimer's Disease. *N. Engl. J. Med.* **368**, 117–127 (2013).
120. Jonsson, T. *et al.* Variant of TREM2 associated with the risk of Alzheimer's disease. *N Engl J Med* **368**, 107–116 (2013).
121. Rosenthal, S. L. *et al.* More evidence for association of a rare TREM2 mutation (R47H) with Alzheimer's disease risk. *Neurobiol. Aging* **36**, 2443.e21-2443.e26 (2015).
122. Slattery, C. F. *et al.* R47H TREM2 variant increases risk of typical early-onset Alzheimer's disease but not of prion or frontotemporal dementia. *Alzheimer's Dement.* **10**, 602–608.e4 (2014).
123. Jin, S. C. *et al.* Coding variants in TREM2 increase risk for Alzheimer's disease. *Hum. Mol. Genet.* **23**, 5838–5846 (2014).
124. Sims, R. *et al.* Rare coding variants in PLCG2, ABI3, and TREM2 implicate microglial-mediated innate immunity in Alzheimer's disease. *Nat. Genet.* (2017). doi:10.1038/ng.3916
125. Bellenguez, C. *et al.* Contribution to Alzheimer's disease risk of rare variants in TREM2, SORL1, and ABCA7 in 1779 cases and 1273 controls. *Neurobiol. Aging* (2017). doi:10.1016/j.neurobiolaging.2017.07.001
126. Hooli, B. V. *et al.* The rare TREM2 R47H variant exerts only a modest effect on Alzheimer disease risk. *Neurology* **83**, 1353–1358 (2014).
127. Jin, S. C. *et al.* TREM2 is associated with increased risk for Alzheimer's disease in African Americans. *Mol. Neurodegener.* **10**, 19 (2015).
128. Miyashita, A. *et al.* Lack of genetic association between TREM2 and late-onset Alzheimer's disease in a Japanese population. *J. Alzheimers. Dis.* **41**, 1031–8 (2014).

129. Yu, J.-T. *et al.* Triggering receptor expressed on myeloid cells 2 variant is rare in late-onset Alzheimer's disease in Han Chinese individuals. *Neurobiol. Aging* **35**, 937.e1-937.e3 (2014).
130. Jiang, T. *et al.* A rare coding variant in TREM2 increases risk for Alzheimer's disease in Han Chinese. *Neurobiol. Aging* **42**, 217.e1-217.e3 (2016).
131. Corder, E. H. *et al.* Gene dose of apolipoprotein E type 4 allele and the risk of Alzheimer's disease in late onset families. *Science* **261**, 921–923 (1993).
132. Rebeck, G. W., Reiter, J. S., Strickland, D. K. & Hyman, B. T. Apolipoprotein E in sporadic Alzheimer's disease: Allelic variation and receptor interactions. *Neuron* **11**, 575–580 (1993).
133. Shi, Y. *et al.* ApoE4 markedly exacerbates tau-mediated neurodegeneration in a mouse model of tauopathy. *Nature* **549**, 523–527 (2017).
134. Rosen, D. R. *et al.* Mutations in Cu/Zn superoxide dismutase gene are associated with familial amyotrophic lateral sclerosis. *Nature* **362**, 59–62 (1993).
135. Bruijn, L. I. *et al.* Aggregation and motor neuron toxicity of an ALS-linked SOD1 mutant independent from wild-type SOD1. *Science* **281**, 1851–4 (1998).
136. Lino, M. M., Schneider, C. & Caroni, P. Accumulation of SOD1 mutants in postnatal motoneurons does not cause motoneuron pathology or motoneuron disease. *J. Neurosci.* **22**, 4825–32 (2002).
137. Pramatarova, A., Laganière, J., Roussel, J., Brisebois, K. & Rouleau, G. A. Neuron-specific expression of mutant superoxide dismutase 1 in transgenic mice does not lead to motor impairment. *J. Neurosci.* **21**, 3369–74 (2001).
138. Boillée, S. *et al.* Onset and progression in inherited ALS determined by motor neurons and microglia. *Science* **312**, 1389–92 (2006).
139. Beers, D. R. *et al.* Wild-type microglia extend survival in PU.1 knockout mice with familial amyotrophic lateral sclerosis. *Proc. Natl. Acad. Sci. U. S. A.* **103**, 16021–6 (2006).
140. Appel, S. H. *et al.* Hematopoietic stem cell transplantation in patients with sporadic amyotrophic lateral sclerosis. *Neurology* **71**, 1326–34 (2008).
141. Zu, T. *et al.* RAN proteins and RNA foci from antisense transcripts in C9ORF72 ALS and frontotemporal dementia. *Proc. Natl. Acad. Sci.* **110**, E4968–E4977 (2013).
142. Liu, Y. *et al.* C9orf72 BAC Mouse Model with Motor Deficits and Neurodegenerative Features of ALS/FTD. *Neuron* **90**, 521–534 (2016).
143. Haeusler, A. R. *et al.* C9orf72 nucleotide repeat structures initiate molecular cascades of disease. *Nature* **507**, 195–200 (2014).

144. Donnelly, C. J. *et al.* RNA Toxicity from the ALS/FTD C9ORF72 Expansion Is Mitigated by Antisense Intervention. *Neuron* **80**, 415–428 (2013).
145. Mori, K. *et al.* The C9orf72 GGGGCC repeat is translated into aggregating dipeptide-repeat proteins in FTL/ALS. *Science* **339**, 1335–8 (2013).
146. DeJesus-Hernandez, M. *et al.* Expanded GGGGCC Hexanucleotide Repeat in Noncoding Region of C9ORF72 Causes Chromosome 9p-Linked FTD and ALS. *Neuron* **72**, 245–256 (2011).
147. Renton, A. E. *et al.* A Hexanucleotide Repeat Expansion in C9ORF72 Is the Cause of Chromosome 9p21-Linked ALS-FTD. *Neuron* **72**, 257–268 (2011).
148. O'Rourke, J. G. *et al.* C9orf72 is required for proper macrophage and microglial function in mice. *Science* **351**, 1324–9 (2016).
149. Freischmidt, A. *et al.* Haploinsufficiency of TBK1 causes familial ALS and frontotemporal dementia. *Nat. Neurosci.* **18**, 631–636 (2015).
150. Dзамко, N., Geczy, C. . & Halliday, G. . Inflammation is genetically implicated in Parkinson's disease. *Neuroscience* **302**, 89–102 (2015).
151. Hamza, T. H. *et al.* Common genetic variation in the HLA region is associated with late-onset sporadic Parkinson's disease. *Nat. Genet.* **42**, 781–785 (2010).
152. MacDonald, M. E. *et al.* A novel gene containing a trinucleotide repeat that is expanded and unstable on Huntington's disease chromosomes. *Cell* **72**, 971–983 (1993).
153. Ross, C. A. & Tabrizi, S. J. Huntington's disease: from molecular pathogenesis to clinical treatment. *Lancet Neurol.* **10**, 83–98 (2011).
154. Björkqvist, M. *et al.* A novel pathogenic pathway of immune activation detectable before clinical onset in Huntington's disease. *J. Exp. Med.* **205**, 1869–77 (2008).
155. Crotti, A. *et al.* Mutant Huntingtin promotes autonomous microglia activation via myeloid lineage-determining factors. *Nat. Neurosci.* **17**, 513–521 (2014).
156. Song, W. *et al.* Alzheimer's disease-associated TREM2 variants exhibit either decreased or increased ligand-dependent activation. *Alzheimer's Dement.* 1–7 (2016). doi:10.1016/j.jalz.2016.07.004
157. Song, W. M. *et al.* Humanized TREM2 mice reveal microglia-intrinsic and -extrinsic effects of R47H polymorphism. *J. Exp. Med.* jem.20171529 (2018). doi:10.1084/jem.20171529
158. Ulland, T. K. *et al.* TREM2 Maintains Microglial Metabolic Fitness in Alzheimer's Disease. *Cell* **170**, 649–663.e13 (2017).

159. Song, W. M. & Colonna, M. The Microglial Response to Neurodegenerative Disease. *Adv. Immunol.* (2018). doi:10.1016/BS.AI.2018.04.002
160. Lin, C.-C. *et al.* Bhlhe40 controls cytokine production by T cells and is essential for pathogenicity in autoimmune neuroinflammation. *Nat. Commun.* **5**, 3551 (2014).
161. Wang, Y. *et al.* TREM2-mediated early microglial response limits diffusion and toxicity of amyloid plaques. *J. Exp. Med.* jem.20151948 (2016). doi:10.1084/jem.20151948
162. Ulrich, J. D. *et al.* Altered microglial response to A β plaques in APPPS1-21 mice heterozygous for TREM2. *Mol. Neurodegener.* **9**, 20 (2014).
163. Doench, J. G. *et al.* Optimized sgRNA design to maximize activity and minimize off-target effects of CRISPR-Cas9. *Nat. Biotechnol.* **34**, 184–191 (2016).
164. Kurosawa, Y. *et al.* Cyclocreatine treatment improves cognition in mice with creatine transporter deficiency. *J. Clin. Invest.* **122**, 2837–2846 (2012).
165. Lin, C.-C. *et al.* IL-1–induced Bhlhe40 identifies pathogenic T helper cells in a model of autoimmune neuroinflammation. *J. Exp. Med.* **213**, 251–271 (2016).